Monthly Notices
of the
ROYAL ASTRONOMICAL SOCIETY

MNRAS **495,** 705–725 (2020)
Advance Access publication 2020 May 4

doi:10.1093/mnras/staa1157

A joint SZ–X-ray–optical analysis of the dynamical state of 288 massive galaxy clusters

A. Zenteno[1★] D. Hernández-Lang,[1,2,3] M. Klein,[2,4] C. Vergara Cervantes,[5] D. L. Hollowood,[6] S. Bhargava,[5] A. Palmese,[7,8] V. Strazzullo,[2,9] A. K. Romer,[5] J. J. Mohr,[2,4] T. Jeltema,[6] A. Saro,[9,10,11] C. Lidman[17] D. Gruen[12,13,14] V. Ojeda,[15] A. Katzenberger,[16] M. Aguena,[18,19] S. Allam,[7] S. Avila,[20] M. Bayliss,[21] E. Bertin,[22,23] D. Brooks,[24] E. Buckley-Geer,[7] D. L. Burke,[13,14] R. Capasso,[25] A. Carnero Rosell,[26] M. Carrasco Kind,[27,28] J. Carretero,[29] F. J. Castander,[30,31] M. Costanzi,[11,32] L. N. da Costa,[19,33] J. De Vicente,[26] S. Desai,[34] H. T. Diehl,[7] P. Doel,[24] T. F. Eifler,[35,36] A. E. Evrard,[37,38] B. Flaugher,[7] B. Floyd,[39] P. Fosalba,[30,31] J. Frieman,[7,8] J. García-Bellido,[20] D. W. Gerdes,[37,38] J. R. Gonzalez,[40] R. A. Gruendl,[27,28] J. Gschwend,[19,33] G. Gutierrez,[7] W. G. Hartley,[24,41,42] S. R. Hinton,[43] K. Honscheid,[44,45] D. J. James,[46] K. Kuehn,[47,48] O. Lahav,[24] M. Lima,[18,19] M. McDonald,[49] M. A. G. Maia,[19,33] M. March,[50] P. Melchior,[51] F. Menanteau,[27,28] R. Miquel,[29,52] R. L. C. Ogando,[19,33] F. Paz-Chinchón,[28,53] A. A. Plazas,[51] A. Roodman,[13,14] E. S. Rykoff,[13,14] E. Sanchez,[26] V. Scarpine,[7] M. Schubnell,[38] S. Serrano,[30,31] I. Sevilla-Noarbe,[26] M. Smith,[54] M. Soares-Santos,[55] E. Suchyta,[56] M. E. C. Swanson,[28] G. Tarle,[38] D. Thomas,[57] T. N. Varga,[2,4] A. R. Walker,[1] and R. D. Wilkinson[5] (DES Collaboration)

Affiliations are listed at the end of the paper

Accepted 2020 April 22. Received 2020 April 21; in original form 2020 April 3

ABSTRACT

We use imaging from the first three years of the Dark Energy Survey to characterize the dynamical state of 288 galaxy clusters at $0.1 \lesssim z \lesssim 0.9$ detected in the South Pole Telescope (SPT) Sunyaev–Zeldovich (SZ) effect survey (SPT-SZ). We examine spatial offsets between the position of the brightest cluster galaxy (BCG) and the centre of the gas distribution as traced by the SPT-SZ centroid and by the X-ray centroid/peak position from *Chandra* and *XMM* data. We show that the radial distribution of offsets provides no evidence that SPT SZ-selected cluster samples include a higher fraction of mergers than X-ray-selected cluster samples. We use the offsets to classify the dynamical state of the clusters, selecting the 43 most disturbed clusters, with half of those at $z \gtrsim 0.5$, a region seldom explored previously. We find that Schechter function fits to the galaxy population in disturbed clusters and relaxed clusters differ at $z > 0.55$ but not at lower redshifts. Disturbed clusters at $z > 0.55$ have steeper faint-end slopes and brighter characteristic magnitudes. Within the same redshift range, we find that the BCGs in relaxed clusters tend to be brighter than the BCGs in disturbed samples, while in agreement in the lower redshift bin. Possible explanations includes a higher merger rate, and a more efficient dynamical friction at high redshift. The red-sequence population is less affected by the cluster dynamical state than the general galaxy population.

★ E-mail: azenteno@ctio.noao.edu

Key words: galaxies: evolution – galaxies: luminosity function, mass function – galaxies: clusters: general.

1 INTRODUCTION

Galaxy cluster mergers are powerful events. The energy released can be up to the order of $\gtrsim 10^{64}$ erg (Sarazin 2002), and the effects of the event can be observed from radio wavelengths, in the form of radio haloes and relics (e.g. Ensslin et al. 1998; Cassano et al. 2010; van Weeren 2011; Drabent et al. 2015; Eckert et al. 2017), to X-ray wavelengths (e.g. Markevitch & Vikhlinin 2007; Takizawa, Nagino & Matsushita 2010; Nelson et al. 2014). Cluster mergers provide unique conditions to study a range of physics, from particle physics, to galaxy evolution and cosmology. They may play a role in accelerating cosmic rays (e.g. van Weeren et al. 2017), generating gamma-rays (e.g. Blasi, Gabici & Brunetti 2007; Pinzke & Pfrommer 2010), and can be used to constrain the dark matter particle self-interaction cross-section (e.g. Markevitch et al. 2004; Harvey et al. 2015; Monteiro-Oliveira et al. 2018). From a cosmological perspective, disturbed clusters provide tests for Λ cold dark matter (ΛCDM; Thompson, Davé & Nagamine 2015; Kim, Peter & Wittman 2017), and they open a window into the past thanks to their enhanced strong lensing efficiency (Zitrin et al. 2013; Acebron et al. 2019).

From the perspective of galaxy evolution, disturbed clusters provide unique environmental conditions under which galaxies are transformed. The abundance of jellyfish galaxies in disturbed clusters (Owers et al. 2012; McPartland et al. 2016) shows that they can be used to examine the effects of the ram pressure from the cluster ICM. Although jellyfish galaxies represent the most spectacular cases, extreme ram pressure may also have an impact on the overall cluster galaxy population. While studies of the cluster luminosity function (LF) abound, studies of the changes in the galaxy population properties as a function of the cluster dynamical state are more scarce. They have been explored in single clusters (e.g. Ma et al. 2010; Pranger et al. 2013, 2014), in samples in the low-mass, low-redshift regime (Ribeiro, Lopes & Rembold 2013; Wen & Han 2015), and in small samples with a higher mass range and wider redshift range (Barrena et al. 2012; De Propris, Phillipps & Bremer 2013). Here, we further improve on such studies by extracting the most extreme cases from a much larger sample, and exploring the highest mass end of the cluster mass function (Bleem et al. 2015; Bayliss et al. 2016), within a wide redshift range.

Classification of disturbed systems can be done using several proxies: for example, the shape of the velocity dispersion (Gaussian versus non-Gaussian; e.g. Martínez & Zandivarez 2012; Ribeiro et al. 2013; de los Rios et al. 2016), the X-ray morphology (e.g. Mohr, Fabricant & Geller 1993; Jeltema et al. 2005; Böhringer et al. 2010; Nurgaliev et al. 2013; Rasia, Meneghetti & Ettori 2013; Parekh et al. 2015; Nurgaliev et al. 2017), diffuse radio emission (e.g. Cassano et al. 2010; Feretti et al. 2012), the cluster galaxy density distribution (e.g. Zitrin et al. 2011; Wen & Han 2015), and a combination of observations at different wavelengths such as the X-ray peak/centroid to brightest cluster galaxy (BCG) offset (e.g. Mann & Ebeling 2012). The use of the BCG position as a proxy for the collisionless component is a logical choice (and less expensive in term of telescope time), as it is expected that the BCG will rapidly sink to the bottom of the potential well due to dynamical friction (Tremaine 1990). This is supported by several observational studies, either when the centre is measured by weak lensing analysis (e.g. Oguri et al. 2010; Zitrin et al. 2012) or by gas based measurements (Lin & Mohr 2004; Hudson et al. 2010; Mann & Ebeling 2012; Song et al. 2012; Rozo & Rykoff 2014). Such studies have shown that the majority of the BCGs lie close to the collisional component (the gas; within 50 h^{-1} kpc), and that the remaining clusters consist of dynamically disturbed systems, with large offsets. Furthermore, hydrodynamical cosmological simulations have also shown that the BCG to dark matter offset is the tightest dynamical state proxy among several studied (Ng et al. 2017; Cialone et al. 2018). In this work, we thus adopt the BCG as the centre of the collisionless component.

Large cluster samples are typically identified using optical, X-ray, and Sunyaev–Zeldovich (SZ) surveys. Currently, large SZ samples of galaxy clusters are available; the *Planck* telescope (Planck Collaboration XXVII 2016), the Atacama Cosmology Telescope (Hasselfield et al. 2013), and the South Pole Telescope (SPT; Bleem et al. 2015) altogether have detected about 2000 galaxy clusters. In this work, we use the SPT cluster sample, and the SZ centroid as a proxy for the collisional component.

The positions of the BCGs are provided by analysing data from the first three years of the Dark Energy Survey (DES; DES Collaboration 2016; Abbott et al. 2018; Morganson et al. 2018). DES is an imaging survey designed to provide constraints on cosmological parameters using four cosmological probes: galaxy clusters, baryon acoustic oscillation, weak lensing, and Type Ia supernovae. To achieve this goal, the final depth (which will come after Year 6) is estimated to be $\sim$24 AB mag in the *grizY* bands over a continuous 5000 deg^2 area in the southern sky including the SPT-SZ survey footprint. This data set is ideal for finding BCGs within the cluster virial radius, and systematically characterizing the cluster galaxy properties and the local background of massive clusters up to redshift $\sim$1.

This paper is organized as follows. In Section 2, we introduce the data and the cluster sample. In Section 3, we describe in detail the dynamical state proxies used. In Section 4, we describe the tools we use to statistically characterize the galaxy population, while in Section 5 we show our results. In Section 6, we present our conclusions.

Throughout this work, we assume a flat ΛCDM cosmology with $H_0 = 68.3$ km s^{-1} Mpc^{-1} and $\Omega_{\rm M} = 0.299$ (Bocquet et al. 2015).

2 DATA AND MEASUREMENTS

2.1 SPT-SZ cluster sample

The cluster sample comes from the 2500 deg^2 SPT-SZ survey. It consists of 516 (387) optically confirmed clusters at signal to noise >4.5(5) (Bleem et al. 2015, hereafter B15). The SPT-SZ cluster sample can be considered as approximately mass selected with a nearly redshift independent mass threshold of $M_{200} > 4 \times 10^{14}$ M$_\odot$. The redshift range extends to $z \approx 1.7$ (Khullar et al. 2019; Strazzullo et al. 2019). We adopt as an estimate of cluster mass $M_{200,\,\rm critical}$, which is the mass within a clustercentric distance of r_{200}, with r_{200} being the radius within which the mean density is 200 times the critical density of the Universe at the cluster redshift. We estimate $\rm M_{200,\,critical}$ from the SZE-based $M_{500,\,\rm critical}$ published in Bleem et al. (2015), adopting the Duffy et al. (2008) mass–concentration relation.

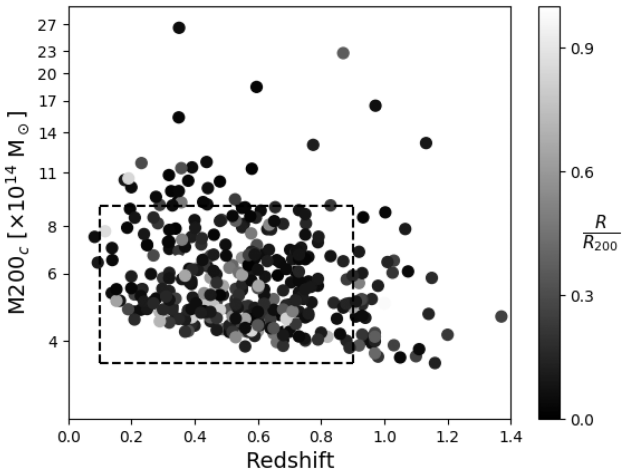

Figure 1. The mass redshift distribution of 368 SPT clusters imaged with DES Y3 data. The dashed box corresponds to limits applied to the SPT-SZ sample to select our sample. In light grey clusters with larger BCG to SZ centroid offset ($D_{\rm BCG\text{-}SZ}$) while the dark points correspond to systems with lower $D_{\rm BCG\text{-}SZ}$.

2.2 DECam optical imaging

Here, we use Dark Energy Camera (DECam; Flaugher et al. 2015) images from the DES Y3 data release, taken from 2013 August 31 to 2016 February 12 (henceforth DESY3; Abbott et al. 2018), covering ∼5000 deg^2. The data are processed through the DES Data Management system (Morganson et al. 2018), which detrends and calibrates the raw DES images, combines individual exposures to create coadded images, and detects and performs photometry of astrophysical objects.

The DES data are key for this study, as they allow us to search for the BCG within the r_{200} for clusters in a wide redshift range. Such a wide redshift range translates into a very different projected radius on the sky. The DES data provides us with complete coverage of r_{200} and a robust estimate of the local galaxy background for each cluster.

We cross-match the SPT-SZ catalogue (at signal to noise >4.5) with the DESY3 Gold sample catalogue (Sevilla-Noarbe, in preparation), excluding clusters with missing information (large gaps, missing bands, bright foreground stars close to the cluster centre, etc.) or bad photometry, finding 368 galaxy clusters. The mean 10(5)σ depth of the multi-object point spread function (PSF) fitting photometry (Drlica-Wagner et al. 2018), and the scatter (1σ) across the cluster fields, are 23.62 ± 0.16 (24.37 ± 0.16), 23.34 ± 0.15 (24.11 ± 0.14), 22.78 ± 0.16 (23.58 ± 0.16), and 22.13 ± 0.16 (22.92 ± 0.16) for *griz*, respectively, providing an average depth of $m^* + 2$ up to redshift 0.66 ± 0.04 (0.83 ± 0.06).

2.3 Redshifts and cluster masses

Clusters redshifts, photometric and spectroscopic, are collected from several sources including Planck Collaboration IX (2011), Sifón et al. (2013), Bleem et al. (2015), and Bayliss et al. (2016). In total there are 110 SPT clusters with spectroscopic redshifts in the SPT-SZ sample (Capasso et al. 2019). The cross-match of the 368 optically cross-matched clusters with the spectroscopic sample renders 104 clusters. The masses adopted here are drawn from B15 and transformed to M_{200}, as described in Section 2.1, and the mass and redshifts distribution of the 368 clusters is shown in Fig. 1.

As we explore the cluster population as a function of dynamical state, we introduce mass–redshift cuts. As we shall see in Section 3, there is a clear tendency for relaxed clusters to be more massive. This is because we selected relaxed clusters using an X-ray proxy, and most of the X-ray data come from a study designed to investigate the most massive systems in SPT (McDonald et al. 2013). These cuts are applied to all samples discussed in this paper. The redshift and mass cuts, designed to limit mass and/or redshift dependencies when comparing sub samples, are $z \in [0.1{:}0.9]$ and $M_{200} < 9 \times 10^{14}$ M$_\odot$. From works such as Hennig et al. (2017) and Martinet et al. (2017), we expect that the impact on the LF from the selection, in that redshift–mass range, will be negligible. These cuts render a final number of 288 clusters, hereafter referred to as the DESY3-SPT sample.

2.4 BCG selection

BCG selection was made in two ways: automatically and by visual inspection of DES images.[1] The latter method involves visually selecting all the potential cluster galaxies within r_{200}, based on several properties including: size, colours, and the number of neighbouring galaxies. We then select the brightest galaxy as the BCG. The automatic method instead proceeds by first fitting a passively evolving simple stellar population (SSP) model, as adopted in Zenteno et al. (2016, hereafter Z16) and in Hennig et al. (2017, hereafter H17),[2] to the red sequence (RS) and then selecting the brightest RS galaxy as the BCG, within r_{200}. More specifically, we first fit the RS model[3] to all galaxies within 0.25 ×r_{200} of the SZ centre and select galaxies with colours that lie within a generous[4] margin of ±0.22 of the RS fit. To find the best RS fit to our model, we use the B15 redshifts as a prior with a delta of ± 0.15. The redshift estimation method employed in B15 is essentially the same as ours, and we do not expect significant differences. The delta of 0.15 is thus a generous margin, a few times the typical difference. Once the best-fitting model is found, we use this RS model to select RS galaxies, within ±0.22 mag in colour within r_{200}, identifying the brightest red galaxy among them. We limit the search at the bright end to $m^* - 4$ to limit foreground contamination. Our experience with SPT clusters has not shown BCGs brighter than that. With these two lists of BCGs, we then inspect the discrepancies to decide, case by case, if the automatic method chose the wrong BCG (e.g. a foreground source with a colour consistent with the RS), or if the visual selection missed a cluster member. This is an iterative process that has involved three of us comparing and checking BCGs, and across several DES data releases and photometric versions. The final BCGs are chosen after this process.

We compare our selection to the RedMaPPer Y3 (RMY3) BCG selection. We match our DESY3-SPT cluster sample to RMY3 using a r_{200} search radius and a richness (λ) > 20 cut, finding 245 matches (85 per cent). Out of the 43 missing systems, 24 are

[1]We use pseudo-colour images using *gri* for clusters at $z < 0.35$ and *riz* for systems above that redshift.
[2]We use the Bruzual & Charlot (2003) synthesis models, assuming a single burst of star formation at $z = 3$ followed by passive evolution to $z = 0$, with six distinct metallicities to match the tilt of the colour–magnitude relation at low redshift. This model correctly reproduces the observed redshift evolution of m^* in the probed redshift range.
[3]We use $g - r$ for $z < 0.30$, $r - i$ for $0.3 \leq z \leq 0.7$, and $i - z$ for $z > 0.7$.
[4]This corresponds to a 3σ average RS scatter in magnitudes (López-Cruz, Barkhouse & Yee 2004), or 3σ intrinsic RS scatter observed in DES data, on SPT clusters, at $z \approx 1$ (Hennig et al. 2017).

in extended areas masked by RM. If we do not consider these, thepercentage of DESY3-SPT clusters identified by RM rises to 93 per cent, with most of the other non-matches being lower mass clusters under different configurations (close to stars or big galaxies, at $z > 0.6$, and even one including a cluster pair in which RM detects just one). From that sample we match the RMY3 BCGs, finding 168 RMY3-SPT BCG matches and 78 mismatches. We then proceed to perform a visual and catalogue inspection of the 78 mismatches to evaluate potential errors. Of the 78 mismatches, 25 correspond to the brightest galaxy within $0.2r_{200}$ from the SPT-SZ centroid, but fainter than our selection within r_{200}, while 45 are just fainter than our BCG candidate. Only 1 RMY3 BCG seems to be undoubtedly a better choice. Our candidate BCG is brighter at the catalogue level, but a visual inspection reveals that this is clearly a mistake. RM used single epoch photometry and it seems that in this case it performed better than the stacked photometry for this particular BCG. Furthermore, there are seven cases in which the BCG selection between RM and ours is different, but they are so similar visually and at catalogue level, that the difference could be accounted for by the different photometric catalogues used. If we discard those cases, we have 70 mismatches, rendering a matching success between our BCG selection and the RM-BCG of 72 per cent. This is consistent with the results of Hoshino et al. (2015), which finds that 20–30 per cent of the RedMaPPer central galaxies are not the brightest cluster member.

We also estimate the level of contamination of our BCG selection statistically. We use the cluster RS to select galaxies brighter than our candidate BCG in a surrounding area equivalent to eight times the cluster area (1–3 r_{200}), filtering stars by using entries with the `EXTENDED_CLASS_MASH_SOF` parameter ≥ 2 (which excludes high confidence stars and candidate stars). This scenario is conservative; no visual inspection was carried out to discard non-galaxy looking candidates and we would not expect a BCG being located that far from the cluster gas component. For 288 clusters, we find zero brighter galaxies for 26 per cent (p_0) of the clusters, for 32 per cent (p_1) we find 1 galaxy brighter, for 23 per cent (p_2) we find 2 galaxies, for 10 per cent (p_3) we find 3 brighter galaxies, for 6 per cent (p_4) we find 4 brighter galaxies, for 2 per cent (p_5) we find 5 brighter galaxies, while for 1 per cent (p_6) we find 6 brighter galaxies. There are no systems with more than six brighter galaxies in the background area used. Adding the probabilities, using the number of RS galaxies brighter than our chosen BCG ($N^{\rm back}_{{\rm BCG},i}$), and normalizing by the area, we find a $P_{\rm tot} = 1 - \sum_{i=0}^{6} p_i \frac{1}{1+N^{\rm back}_{{\rm BCG},i}/8} = 14$ per cent chance of BCG miss-identification over the whole sample.

Finally, we test the accuracy of the method by cross-matching our BCGs to spectroscopic redshifts found in the literature as described in Section 2.3 (Bayliss et al. 2014, 2016; Capasso et al. 2019). We match the BCG sample and the spectroscopic samples within 2 arcsec, finding 68 candidate BCGs with redshifts. From this match we find only one system with an inconsistent redshift; SPT-CLJ2301-4023 has a BCG with a redshift of 0.778069 while the cluster redshift is 0.8349. A visual inspection reveals that the BCG belongs to the RS and looks like a cluster member surrounded by several other cluster members with the same colour. The spectroscopic BCG is also red and bright with a magnitude consistent with the visual BCG within the photometric error bars. Extrapolating to the whole sample, this implies that about 2 per cent of the BCGs selected with our procedure may be misidentified. We further test our BCG selection in Section 5.1.1.

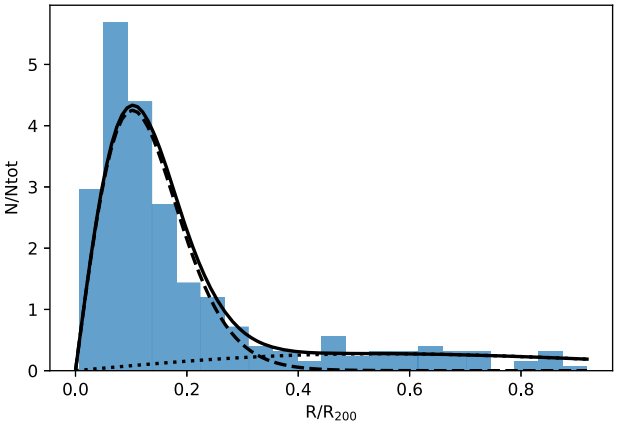

Figure 2. Normalized histogram of the BCG-SZ offset distribution. The $D_{\rm BCG\text{-}SZ}$ distribution can be described as the sum (black line) of a relaxed distribution (dashed line) plus a disturbed distribution (dotted line) The disturbed sample consists of the clusters with $R > 0.4 \times r_{200}$ and $D_{\rm BCG\text{-}SZ} > 3\Delta\theta$.

2.5 X-ray data

2.5.1 Chandra

The *Chandra* X-ray Visionary Project (XVP; PI B. Benson) published X-ray data of 90 SPT systems, at $0.35 < z < 1.2$, and their properties have been characterized in several papers (e.g. Semler et al. 2012; McDonald et al. 2014), including cool-core properties (McDonald et al. 2013) and a morphological classification (Nurgaliev et al. 2017), which are relevant for this study. The matching of the Nurgaliev et al. (2017) sample with DESY3-SPT renders 41 clusters within our redshift–mass limits (DESY3-XVP sample hereafter).

We also make use of *Chandra* public data by using the Mass Analysis Tool for *Chandra* (MATCha) pipeline (Hollowood et al. 2019). Given an input cluster catalogue, this code queries the *Chandra* archive and reduces all public data for clusters in the catalogue. The output of MATCha includes measurements of cluster T_X, L_X, and X-ray centroid within a set of apertures, 500 kpc, r_{2500}, r_{500}, and core-cropped r_{500}. The position of the X-ray peak is estimated as the brightest pixel after smoothing with a Gaussian of 50 kpc width (see Hollowood et al. 2019, for details). Matching the MATCha program results to our DESY3-SPT sample we obtain 39 matches, 1 of them a new addition to our sample.

In total, we find 42 systems with *Chandra* data in the DESY3-SPT sample.

2.5.2 XMM–Newton

We also searched for counterparts in the *XMM–Newton* (*XMM*) space telescope archive. The *XMM* analysis was performed using an adaptation of the X-ray Automated Pipeline Algorithm (Freeman et al. 2002) developed for the *XMM* Cluster Survey (XCS, e.g. Romer et al. 2000). XCS uses all available X-ray data in the *XMM* Science Archive to search for galaxy clusters that were detected first in *XMM* images. X-ray sources are detected in *XMM* images using an algorithm based on wavelet transformations (e.g. Lloyd-Davies et al. 2011), and then compared to the position-dependent PSF to classify them as extended, PSF-sized, or point like. Most of the extended X-ray sources are clusters, therefore all extended sources

are flagged as cluster candidates, but in some cases these can be low-redshift galaxies, supernova remnants or multiple blended point sources. We then cross-match the DESY3-SPT clusters and XCS cluster candidates. We made the following assumptions: all physical matches will occur within 1.5 Mpc of the SPT centre (assuming that the X-ray source to be at the SPT redshift), and all physical matches will be contained within the sub-set of XCS sources that are defined as being extended and with more than 100 photon counts. Not all of the DESY3-SPT clusters in the *XMM* footprint will have such counterparts in XCS because either (i) the different cluster finding methodology employed by the two surveys, or (ii) the respective *XMM* observation has a low exposure time and/or high background, or (iii) the SPT cluster falls on the edge of the field of view and/or in an EPIC chip gap. This procedure renders 43 matches. From those 43 matches, 28 are found in the DESY3-SPT sample; 25 of them provide new X-ray information to add to the *Chandra* list.

The final list of clusters with X-ray information in the DESY3-SPT sample is 67.

3 DYNAMICAL STATE PROXIES

As clusters grow, by merging with other clusters or groups, the gas, dark matter, and galaxy components depart from relaxation. Therefore, signatures of that departure can be identified by using a gas proxy and a (dark) matter proxy. Here, we describe the combination of X-ray, SZ and optical imaging proxies used to classify the clusters' dynamical state.

3.1 Disturbed sample

3.1.1 BCG-SZ centroid offset

We use the offset between the BCG and the SPT-SZ centroid to classify clusters with the largest offsets as disturbed. Specifically, we select all clusters that have a BCG-SZ offset of $D_{\rm BCG\text{-}SZ} > 0.4 \times r_{200}$. The choice of $0.4 \times r_{200}$ is taken after plotting the $D_{\rm BCG\text{-}SZ}$ histogram distribution, which looks flat after $\sim 0.4 \times r_{200}$ (see Fig. 2). We also take into account the SPT positional uncertainty $\Delta\theta$, which is defined by $\sqrt{(\theta^2_{\rm beam} + (k\theta_{\rm c})^2)}/\xi$, where ξ is the significance of the cluster SZ detection, $\theta_{\rm beam}$ is the beam FWHM, $\theta_{\rm c}$ is the core radius, and k is a factor of the order of unity (see Story et al. 2011; Song et al. 2012). A cluster is included in the disturbed sample if $D_{\rm BCG\text{-}SZ} > 3\Delta\theta$. We find 39 systems that satisfy both conditions.

3.1.2 X-ray cluster morphology: A_{phot}

The bulk of the merging cluster samples studied in this work are identified through the $D_{\rm BCG\text{-}SZ}$ selection. We extend these samples using X-ray information. For the XVP sample, Nurgaliev et al. (2017) computed the photon asymmetry index ($A_{\rm phot}$; Nurgaliev et al. 2013). $A_{\rm phot}$ measures the deviation from axisymmetry of the X-ray emission.

Using the $A_{\rm phot} > 0.6$ for disturbed clusters, we find that seven systems that fall into this category,[5] one is present in our BCG-SZ selection. Several of $A_{\rm phot}$ selected disturbed clusters also present clear substructures in the red galaxy density maps. Visual inspection of the DES images confirm that the position of the BCGs in these six clusters is close to the SZ centroid, explaining the low $D_{\rm BCG\text{-}SZ}$. This may indicate a different merging phase in comparison to the $D_{\rm BCG\text{-}SZ}$ selected systems, a projection effect, or a case of a minor merger that manages to disturb the gas but not the BCG.

[5] An eighth cluster with a high $A_{\rm phot}$ value, SPT-CLJ2332-5053, is excluded from this selection. Inspection of the *Chandra* image shows that the high $A_{\rm phot}$ value is due to contamination from SPT-CLJ2331-5051, a companion cluster possibly in a pre-merger stage.

3.1.3 BCG-X-ray centroid/peak offset

Using $D_{\rm BCG\text{-}X} > 0.4\ r_{200}$, and assuming negligible X-ray centroid/peak positional uncertainty, on *Chandra* data, we find one new system, SPT-CLJ0346−5439, a cluster with a $D_{\rm BCG\text{-}SZ}$ of $0.37 r_{200}$. In the case of the *XMM* sub-sample, we also add one cluster, SPT-CLJ0253−6046 at a $D_{\rm BCG\text{-}SZ}$ of $0.36 r_{200}$, to the disturbed sample.

3.2 Relaxed sample

To highlight the changes in the galaxy populations due to the dynamical state, we create a relaxed sample. Due to the large SZ centroid positional uncertainty, the BCG-SZ-centroid offset is not a good proxy to create such a sample. We turn here exclusively to the clusters with X-ray information.

We define a system as relaxed if any of the following three conditions is met: (i) the cluster has $A_{\rm phot} \leq 0.1$; (ii) the cluster is classified as having a cool-core (systems with $K_0 < 30$ keV cm^2; McDonald et al. 2013); or (iii) the BCG satisfies $D_{\rm BCG\text{-}X} < 42(71)$ kpc to the X-ray peak (centroid) (Mann & Ebeling 2012).

3.2.1 X-ray morphology: A_{phot}

Applying the Nurgaliev et al. (2017) selection for relaxed systems ($A_{\rm phot} \leq 0.1$), we find 15 clusters that satisfy this condition.

3.2.2 Cool-core clusters

We use cool-core SPT-SZ clusters reported in McDonald et al. (2013), which are defined as systems with $K_0 < 30$ keV cm^2. This results in 16 clusters within our redshift–mass limits. These 16 clusters include 9 already selected by the $A_{\rm phot} \leq 0.1$ criterion.

3.2.3 BCG-X-ray centroid/peak offset

The X-ray centroid/peak to BCG offset is a well-known predictor of the dynamical state of a cluster. We use the X-ray centroid and peak to BCG distance to complement the morphology and cool-core samples. To select relaxed systems, we follow Mann & Ebeling (2012); we use $D_{\rm BCG\text{-}X} < 42$ kpc if we use the X-ray peak, and $D_{\rm BCG\text{-}X} < 71$ kpc if we use the X-ray centroid. We add 12 clusters from the *XMM* data and 11 from *Chandra* data to this sample.

We note that the conditions described in Sections 3.2.2 and 3.2.3 also include clusters classified as disturbed; SPT-CLJ0102−4603, SPT-CLJ0252−4828, SPT-CLJ0346−5439, and SPT-CLJ2218−4519. These systems are excluded from both the relaxed and disturbed samples. SPT-CLJ0102−4603 is identified as a cool-core cluster with $K_0 = 10.3^{+6.1}_{-5.8}$ keV cm^2, a $D_{\rm BCG\text{-}X} < 42$ kpc to peak, but an $A_{\rm phot}$ of $0.68^{+0.18}_{-0.17}$. Visual inspection of the X-ray image of SPT-CLJ0102−4603 reveals some signs of asymmetry. It is conceivable that the cluster suffered a recent minor merger, without disturbing the core. SPT-CLJ0252−4824 is selected as a relaxed system due to $D_{\rm BCG\text{-}X} = 0.03$ kpc to the X-ray peak flux, but it is also classified as disturbed with an $A_{\rm phot}$ of $0.97^{+0.34}_{-0.28}$. Visual

Table 1. Disturbed DESY3-SPT cluster sample.

Name	SPT RA (J2000.0)	SPT Dec. (J2000.0)	BCG RA (J2000.0)	BCG Dec. (J2000.0)	Redshift	M_{200} $10^{14}\,h_{70}^{-1}\,M_\odot$	R_{200} (arcmin)	Offset R_{200}
SPT-CLJ0014−4952	3.6969	−49.8772	3.70284	−49.88481[a]	0.752	8.10	3.27	0.10
SPT-CLJ0038−5244	9.7204	−52.7390	9.74027	−52.76584	0.42	4.79	4.16	0.42
SPT-CLJ0107−4855	16.8857	−48.9171	16.86943	−48.88841	0.60	4.24	3.08	0.60
SPT-CLJ0111−5518	17.8446	−55.3138	17.89407	−55.31981	0.56	4.23	3.23	0.53
SPT-CLJ0131−5604	22.9331	−56.0821	22.87732	−56.10802	0.69	6.17	3.17	0.77
SPT-CLJ0135−5904	23.9753	−59.0814	23.99831	−59.10447	0.49	4.28	3.57	0.44
SPT-CLJ0144−4807	26.1795	−48.1281	26.10096	−48.13661	0.31	4.80	5.27	0.60
SPT-CLJ0145−5301	26.2645	−53.0295	26.49096	−53.18341	0.117	7.73	14.25	0.87
SPT-CLJ0147−5622	26.9652	−56.3779	26.99103	−56.33408	0.64	4.54	3.01	0.92
SPT-CLJ0151−5654	27.7898	−56.9110	27.67812	−56.88732	0.29	4.75	5.54	0.71
SPT-CLJ0152−5303	28.2342	−53.0540	28.26770	−53.08393	0.55	6.59	3.79	0.57
SPT-CLJ0212−4657	33.1061	−46.9502	33.12022	−46.94882[a]	0.655	8.93	3.71	0.07
SPT-CLJ0217−4310	34.4138	−43.1819	34.40557	−43.15638	0.52	6.30	3.89	0.40
SPT-CLJ0253−6046	43.4619	−60.7725	43.45072	−60.74986	0.45	4.60	3.90	0.45[b]
SPT-CLJ0256−5617	44.0997	−56.2980	44.08792	−56.30314[a]	0.58	6.83	3.70	0.07
SPT-CLJ0257−4817	44.4463	−48.2970	44.48667	−48.33896	0.46	4.95	3.93	0.76
SPT-CLJ0257−5842	44.3934	−58.7107	44.42008	−58.66096	0.44	5.05	4.09	0.76
SPT-CLJ0304−4748	46.1503	−47.8115	46.16431	−47.78205	0.51	6.20	3.93	0.47
SPT-CLJ0307−6225	46.8336	−62.4327	46.84936	−62.40283[a]	0.579	7.63	3.84	0.48
SPT-CLJ0313−5645	48.2620	−56.7548	48.29124	−56.74206	0.66	3.96	2.82	0.44
SPT-CLJ0337−4928	54.4573	−49.4738	54.43516	−49.51382	0.53	5.14	3.59	0.71
SPT-CLJ0337−6300	54.4692	−63.0103	54.53705	−63.05146	0.48	4.81	3.77	0.82
SPT-CLJ0354−5904	58.5612	−59.0733	58.61676	−59.09708	0.41	6.19	4.61	0.48
SPT-CLJ0403−5719	60.9681	−57.3237	60.91901	−57.28362	0.466	5.58	4.05	0.71
SPT-CLJ0422−4608	65.7490	−46.1436	65.76715	−46.18128	0.70	4.36	2.79	0.85
SPT-CLJ0429−5233	67.4315	−52.5609	67.39019	−52.54447	0.53	4.08	3.32	0.54
SPT-CLJ0439−5330	69.9290	−53.5038	69.90064	−53.53884	0.43	5.32	4.23	0.55
SPT-CLJ0451−4952	72.9661	−49.8796	72.96825	−49.93968	0.39	4.60	4.34	0.83
SPT-CLJ0522−5026	80.5159	−50.4394	80.54907	−50.41640	0.52	4.62	3.51	0.53
SPT-CLJ0526−5018	81.5087	−50.3147	81.53626	−50.27385	0.58	4.25	3.15	0.85
SPT-CLJ0550−5019	87.5504	−50.3236	87.56539	−50.34343	0.65	4.17	2.90	0.46
SPT-CLJ0551−5709	87.9041	−57.1557	87.88328	−57.16026[a]	0.423	7.42	4.79	0.09
SPT-CLJ0600−4353	90.0614	−43.8879	90.07561	−43.93144	0.36	7.35	5.40	0.50
SPT-CLJ0611−4724	92.9212	−47.4111	92.86097	−47.40201	0.49	5.56	3.90	0.64
SPT-CLJ0612−4317	93.0249	−43.2992	93.06164	−43.30627	0.54	6.02	3.73	0.44
SPT-CLJ2040−5342	310.2194	−53.7116	310.24179	−53.74783	0.55	5.94	3.66	0.63
SPT-CLJ2140−5331	325.0330	−53.5178	325.01766	−53.48353	0.56	4.56	3.31	0.64
SPT-CLJ2146−5736	326.6957	−57.6148	326.75290	−57.63592	0.602	5.57	3.36	0.66
SPT-CLJ2228−5828	337.2153	−58.4686	337.17177	−58.47420	0.71	4.77	2.85	0.49
SPT-CLJ2242−4435	340.5195	−44.5897	340.55949	−44.59951	0.73	4.10	2.66	0.68
SPT-CLJ2254−5805	343.5895	−58.0851	343.39591	−58.10217	0.153	5.08	9.75	0.64
SPT-CLJ2344−4224	356.1481	−42.4100	356.10884	−42.46793	0.29	4.49	5.44	0.71
SPT-CLJ2358−6129	359.7075	−61.4862	359.70022	−61.43302	0.37	5.92	4.92	0.65

[a]Clusters with a BCG candidate in McDonald et al. (2016). Due to the McDonald et al. (2016) selection procedure, the BCGs presented for these five cases are different than what is reported here. See Section 2.4 for details.
[b]The offset reported corresponds to the distance between the BCG and X-ray centroid.

inspection of the X-ray image reveals clear signs of merging activity, with the gas having a filamentary structure, while the candidate BCG is clearly dominant and unique. In the case of SPT-CLJ0346−5439, we find a cluster with a $K_0 < 30$ keV cm^2, $D_{\rm BCG\text{-}SZ} = 0.43 r_{200}$, and a large BCG-X-ray offset. X-ray images reveal an ellipsoidal photon distribution, not much different than other clusters, while having two dominant BCGs, a central one and our candidate 0.34 mag brighter (∼50 times the photometric error). In the case of SPT-CLJ2218−4519, $A_{\rm phot}$ defines it as a relaxed cluster ($0.08^{+0.05}_{-0.08}$) but has a large $D_{\rm BCG\text{-}X}$ value ($0.54 r_{200}$). The X-ray imaging shows a regular photon distribution confirming the $A_{\rm phot}$ value. Furthermore, a visual and catalogue inspection of the candidate BCG and bright galaxies close to the X-ray emission reveals that there may be a potential error in the catalogue magnitudes and that the BCG may be miss-identified.

The final disturbed cluster sample is composed of 43 clusters (listed in Table 1), while the final relaxed cluster sample has 41 (listed in Table 2), with half of them at $z \gtrsim 0.6$, a redshift scarcely probed by previous studies. The mass and redshift distribution of both cluster samples, within the mass and redshift cuts described in Section 2.3, is shown in Fig. 3. Images for a sub sample of 12 disturbed systems and 12 relaxed systems can be seen in Fig. 4.

We also create an intermediate sample of clusters, numbering 204, consisting of all clusters that remain. Note that such sample will contain disturbed and relaxed clusters (i.e. our disturbed and relaxed samples are by no means complete).

Table 2. Relaxed DESY3-SPT cluster sample.

Name	SPT RA (J2000.0)	SPT Dec. (J2000.0)	BCG RA (J2000.0)	BCG Dec. (J2000.0)	Redshift	M_{200} $10^{14}\,h_{70}^{-1}\,M_\odot$	R_{200} (arcmin)	Offset R_{200}
SPT-CLJ0000−5748	0.2499	−57.8064	0.25015	−57.80931[a]	0.702	6.91	3.25	0.01
SPT-CLJ0033−6326	8.4767	−63.4463	8.50134	−63.43077[b]	0.597	7.12	3.67	0.02
SPT-CLJ0058−6145	14.5799	−61.7635	14.58415	−61.76683[a]	0.83	6.65	2.87	0.03
SPT-CLJ0123−4821	20.7923	−48.3588	20.79565	−48.35626[a]	0.655	6.73	3.38	0.01
SPT-CLJ0200−4852	30.1436	−48.8757	30.14204	−48.87127[a]	0.498	7.13	4.18	0.01
SPT-CLJ0230−6028	37.6418	−60.4689	37.63540	−60.46297	0.68	5.41	3.06	0.02
SPT-CLJ0231−5403	37.7768	−54.0563	37.77771	−54.06232	0.59	4.87	3.26	0.03
SPT-CLJ0232−5257	38.1876	−52.9578	38.17795	−52.95628[b]	0.556	8.08	4.03	0.22
SPT-CLJ0243−5930	40.8615	−59.5124	40.86283	−59.51725[a]	0.635	6.92	3.48	0.00
SPT-CLJ0257−5732	44.3506	−57.5426	44.33722	−57.54837	0.434	4.73	4.04	0.02
SPT-CLJ0307−5042	46.9516	−50.7071	46.96054	−50.70122[a]	0.55	7.92	4.03	0.04
SPT-CLJ0310−4647	47.6291	−46.7834	47.63545	−46.78566[a]	0.709	6.53	3.17	0.02
SPT-CLJ0317−5935	49.3216	−59.5851	49.31598	−59.59140	0.469	5.96	4.12	0.01
SPT-CLJ0324−6236	51.0530	−62.6021	51.05100	−62.59883[a]	0.750	7.57	3.21	0.01
SPT-CLJ0334−4659	53.5464	−46.9932	53.52817	−46.98379[b]	0.485	8.29	4.48	0.24
SPT-CLJ0342−5354	55.5220	−53.9118	55.51920	−53.92059	0.53	5.11	3.58	0.02
SPT-CLJ0343−5518	55.7617	−55.3032	55.75973	−55.31195	0.55	5.61	3.59	0.04
SPT-CLJ0352−5647	58.2367	−56.7996	58.23958	−56.79772[a]	0.649	6.41	3.34	0.02
SPT-CLJ0406−4805	61.7275	−48.0866	61.73024	−48.08254[a]	0.737	7.01	3.16	0.01
SPT-CLJ0406−5455	61.6906	−54.9210	61.68571	−54.92573	0.74	5.23	2.86	0.05
SPT-CLJ0439−4600	69.8087	−46.0142	69.80806	−46.01358	0.34	7.86	5.77	0.03
SPT-CLJ0441−4855	70.4511	−48.9190	70.44958	−48.92335[a]	0.79	7.23	3.05	0.02
SPT-CLJ0509−5342	77.3374	−53.7053	77.33914	−53.70351[a]	0.461	7.57	4.52	0.01
SPT-CLJ0528−5300	82.0196	−53.0024	82.02214	−52.99814[a]	0.768	5.53	2.84	0.01
SPT-CLJ0533−5005	83.4009	−50.0901	83.41447	−50.08449[b]	0.881	5.78	2.64	0.29
SPT-CLJ0542−4100	85.7167	−41.0044	85.70855	−41.00012[a]	0.642	7.82	3.60	0.01
SPT-CLJ0559−5249	89.9251	−52.8260	89.93006	−52.82419[a]	0.609	8.76	3.88	0.04
SPT-CLJ2011−5725	302.8527	−57.4217	302.86241	−57.41971[a]	0.279	5.16	5.88	0.01
SPT-CLJ2022−6323	305.5261	−63.3989	305.53709	−63.39950	0.383	6.17	4.85	0.01
SPT-CLJ2043−5035	310.8284	−50.5938	310.82312	−50.59232[a]	0.723	6.88	3.18	0.01
SPT-CLJ2055−5456	313.9957	−54.9368	313.98389	−54.92727	0.139	6.99	11.80	0.01
SPT-CLJ2130−6458	322.7280	−64.9767	322.73421	−64.97787	0.316	7.25	5.96	0.02
SPT-CLJ2134−4238	323.5020	−42.6438	323.50290	−42.64810	0.196	8.85	9.45	0.02
SPT-CLJ2148−6116	327.1812	−61.2780	327.16178	−61.26553[b]	0.571	6.70	3.71	0.02
SPT-CLJ2222−4834	335.7122	−48.5735	335.71118	−48.57642[a]	0.652	8.22	3.62	0.01
SPT-CLJ2232−5959	338.1487	−59.9903	338.14086	−59.99810[a]	0.594	8.39	3.89	0.00
SPT-CLJ2233−5339	338.3295	−53.6502	338.31500	−53.65259[a]	0.440	8.23	4.81	0.04
SPT-CLJ2259−6057	344.7528	−60.9546	344.75411	−60.95951[a]	0.75	8.57	3.34	0.01
SPT-CLJ2331−5051	352.9608	−50.8639	352.96306	−50.86496[ac]	0.576	8.46	3.99	0.00
SPT-CLJ2332−5358	353.1057	−53.9675	353.11446	−53.97442	0.402	7.89	5.08	0.01
SPT-CLJ2352−4657	358.0631	−46.9569	358.06778	−46.96021[a]	0.73	6.71	3.14	0.00

[a]Same BCG candidate visually selected in McDonald et al. (2016).
[b]Different BCG candidate selected in McDonald et al. (2016) due to the selection procedure. See Section 2.4 for details.
[c]Cluster in pre-merging event.

We also tested an optical proxy for the cluster dynamical state. We used the Wen & Han (2015) recipe, but we were unable to find consistent results, when comparing to samples created using X-ray data for dynamical state estimation. We will explore other dynamical state proxies in follow-up papers.

4 GALAXY POPULATIONS

4.1 Luminosity function

Following Z16, we construct individual cluster LFs using galaxies within a projected r_{200}, centred on the BCG, and performing a statistical background subtraction using the background region within 1.5 and $3r_{200}$. For two populations; RS galaxies and all cluster galaxies, we use the same BCG to set the bright limit of the LF, independently of its colour. The projected, background-corrected LF is then de-projected using an NFW profile with a concentration of 3 ($c_{\rm corr}$), a value in between the findings of Z16 and H17 for SPT clusters in different mass ranges. We use 0.5 mag bins for the LF, and scaled it by the cluster volume in $\rm Mpc^3$. The BCG is excluded from the LF.

As in Z16 and H17, for all stars with a 2MASS J-band magnitude $m_J < 14$, in both the cluster and background regions, we mask the area within a distance from the star depending on the star's magnitude.[6]

[6]We use a radius $= 10^{(A_J + B_J \times J\ \rm band)}$ arcseconds, with $A_J = 2.4378$, and $B_J = -0.10576$.

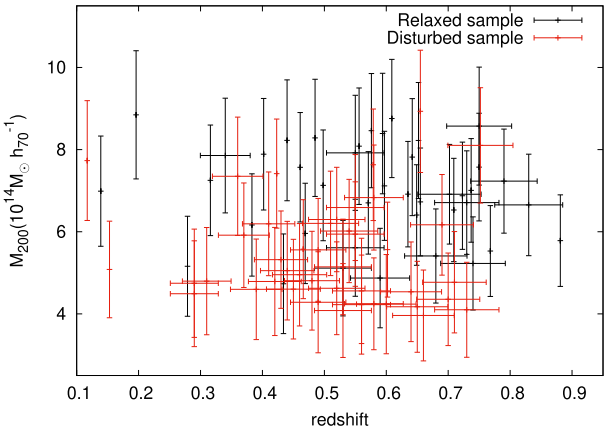

Figure 3. The location of relaxed (41) and disturbed (43) cluster sample mass–redshift plane. The mass and redshift cuts described in Section 2.3 have been applied. It can be seen that the average mass of the relaxed clusters are higher than the average mass of the disturbed clusters.

Corrections due to masked regions and background oversubtraction (from cluster members at $r > 1.5\ r_{200}$) are applied here as well. In the case of cluster masked regions (within r_{200}), we correct for the missing cluster galaxies using the NFW profile with the concentration $c_{\rm corr}$. Also, using the same model, we correct for the over subtraction due to cluster galaxies contaminating the background dominated region (also corrected by masked areas). This over subtraction can be expressed mathematically in terms of the observables that we measure $\bar{N}^{1.5<r'<3}$ and $\bar{N}^{r'<1}$, corresponding to the galaxies at $1.5 < r' < 3$, and the galaxies within $r' < 1$, respectively, where $r' = r/r_{200}$. Both cluster galaxies and background galaxies contribute to these numbers:

$$\bar{N}^{1.5<r'<3} = N_{\rm back}^{1.5<r'<3} + N_{\rm clus}^{1.5<r'<3} \quad (1)$$

and

$$\bar{N}^{r'<1} = N_{\rm back}^{r'<1} + N_{\rm clus}^{r'<1}. \quad (2)$$

Our first step is to create the LF by subtracting those two observables:

$$N_{\rm clus,LF}^{r'<1} = \bar{N}^{r'<1} - A_{\rm N} \times \bar{N}^{1.5<r'<3}, \quad (3)$$

where $A_{\rm N}$ is the area normalization. Replacing above equation with (1) and (2) we obtain

$$N_{\rm clus,LF}^{r'<1} = N_{\rm back}^{r'<1} + N_{\rm clus}^{r'<1} - A_{\rm N} \times \left(N_{\rm back}^{1.5<r'<3} + N_{\rm clus}^{1.5<r'<3}\right),$$

which can be simplified by cancelling the background contribution ($N_{\rm back}^{r'<1} = A_{\rm N} \times N_{\rm back}^{1.5<r'<3}$):

$$N_{\rm clus,LF}^{r'<1} = N_{\rm clus}^{r'<1} - A_{\rm N} \times N_{\rm clus}^{1.5<r'<3}. \quad (4)$$

This equation shows the oversubtraction term introduced in equation (3). To correct for this we use a NFW profile to connect cluster galaxies at different radii:

$$N_{\rm clus}^{1.5<r'<3} = \tau(c_{\rm corr}) \times N_{\rm clus}^{r'<1}.$$

Using this relation in equation (4), we obtain a coefficient we can use to correct such oversubtraction:

$$N_{\rm clus,LF}^{r'<1} = N_{\rm clus}^{r'<1} - A_{\rm N} \times \tau(c_{\rm corr}) \times N_{\rm clus}^{r'<1},$$

$$N_{\rm clus,LF}^{r'<1} = N_{\rm clus}^{r'<1}(1 - A_{\rm N} \times \tau(c_{\rm corr})),$$

$$N_{\rm clus}^{r'<1} = \frac{N_{\rm clus,LF}^{r'<1}}{(1 - A_{\rm N} \times \tau(c_{\rm corr}))} = C \times N_{\rm clus,LF}^{r'<1}.$$

The average correction C is 1.06 with a maximum of 1.085. The correction boosts the number of galaxies within r_{200} to compensate for the oversubtraction of cluster galaxies at $1.5 < r' < 3$. We notice that these corrections are expected to be well defined for the relaxed systems as the galaxy distribution is expected to have a NFW shape. In the case of the disturbed cluster sample, the suitability of the corrections are less clear. If the clusters have a lower concentration due to a recent merger, such a correction would underestimate the contamination of cluster galaxies in the background area, underestimating the cluster richness.

4.1.1 *Completeness*

The DES data used in this paper provides a homogeneous data set to a depth of 23.62 ± 0.16, 23.34 ± 0.15, 22.78 ± 0.16, and 22.13 ± 0.16 in *griz* at 10σ, as measured in our 84 clusters. For clusters at $z > 0.45(0.65)$, the average photometry of $m^* + 3(2)$ galaxies has a signal-to-noise ratio less than 10. For these cases, completeness becomes important and we adopt correction factors to enable analysis to a common depth relative to the cluster galaxy LF characteristic magnitude.

The correction follows our previous work in Zenteno et al. (2011): we compare the galaxy number counts in the *griz* bands in an annulus of radii 1.5–3 r_{200} around each cluster, to the deeper Canada–France–Hawaii Telescope Legacy Survey (CFHTLS; Brimioulle et al. 2008, private communication)[7] by dividing the number count histogram in the cluster field by that in the CFHTLS field. If the ratio is well behaved (i.e. is stable around 1 before the completeness correction is needed, and the 10σ error in the catalogue is consistent with the 90 per cent completeness from the divided histograms), we fit the resulting curve with an error function which is used to account for the missing objects as we approach the 50 per cent completeness depth (no data is used beyond 50 per cent completeness limit). If the curve is not well behaved, we use the data up to 90 per cent completeness, defined by the catalogue errors. As noted in Section 2.2, given the average photometric depth, this completeness correction allows us to reach $m^* + 3$ up to redshift 0.61 ± 0.04, or $m^* + 2$ up to redshift 0.83 ± 0.06.

4.1.2 *Stacked luminosity function*

To stack the data we bring each individual LF, extracted to up to $m^* + 3$, to the same magnitude frame. We do this by subtracting from the cluster LF bins, in apparent magnitudes, the SSP model m^* magnitude given the cluster redshift (see Section 2.4). Once the data are brought to this common frame, they are stacked using the inverse variance weighted average method used in Z16:

$$N_j = \frac{\sum_i N_{ij}^{z=0}/\sigma_{ij}^2}{\sum_i 1/\sigma_{ij}^2},$$

where $N_{ij}^{z=0}$ is the number of galaxies per cubic Mpc per magnitude bin at redshift zero, in the jth bin corresponding to the ith cluster

[7]Count histograms correspond to the D-1 1 deg^2 field, at $l = 172.0°$ and $b = -58.0°$ with a magnitude limit beyond $r = 27$ and a seeing better than 1.0 arcsec.

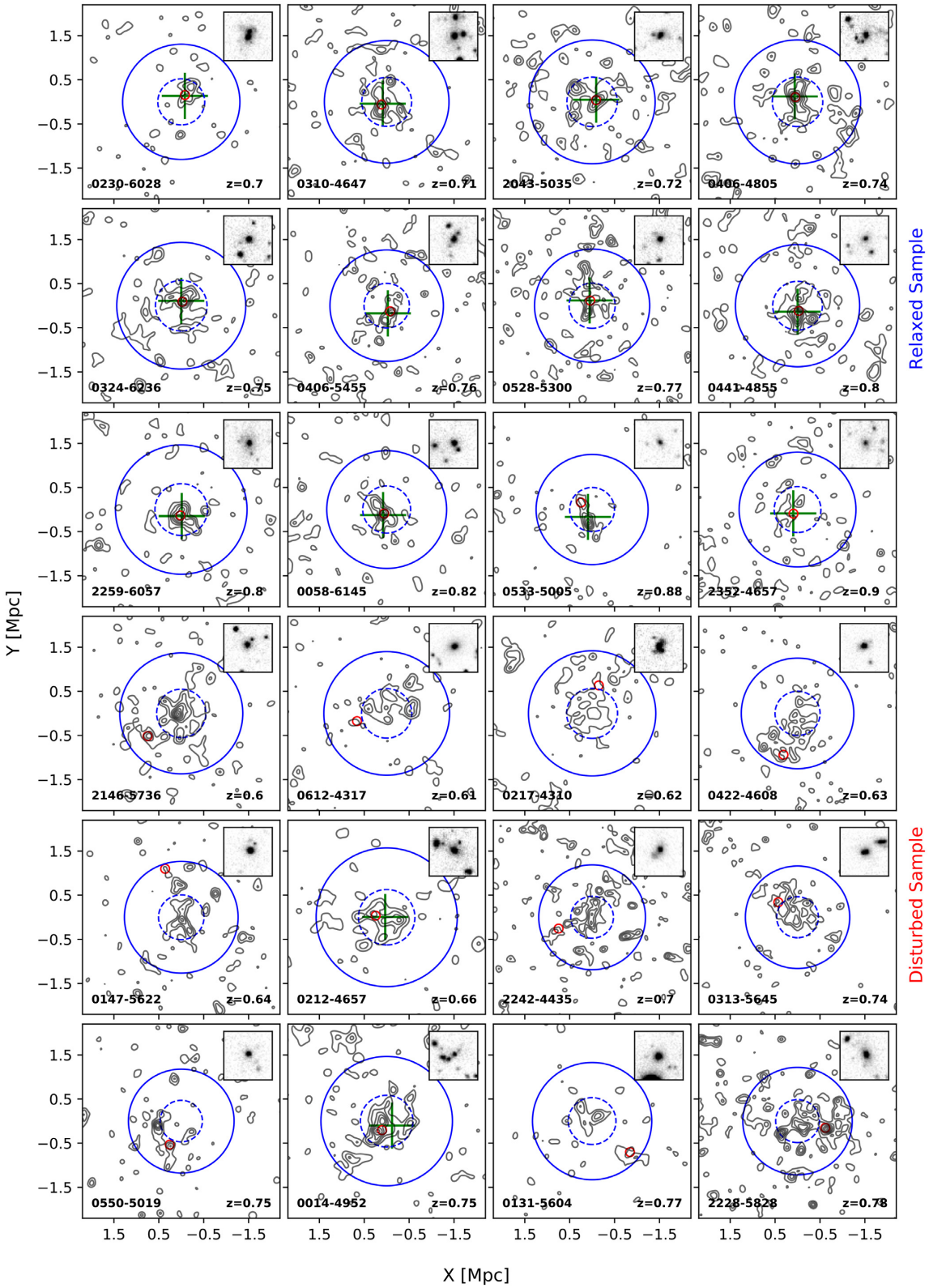

Figure 4. The top 12 clusters correspond to the highest redshift relaxed systems. The outer circled represents r_{200}, while the inner circle corresponds to $0.4r_{200}$. Contours correspond to the RS galaxy distribution. The green cross shows the X-ray peak emission while *i*-band images of the BCG is shown in the top right corner. The relaxed systems are selected if the BCG is within 42/71 kpc of the X-ray peak/centroid (Mann & Ebeling 2012), if $K_0 < 30$ keV cm^2 (McDonald et al. 2013), or if it is classified as relaxed by its morphology with a $A_{\rm phot} \leq 0.1$ (Nurgaliev et al. 2017). The bottom 12 clusters correspond to the highest redshift disturbed systems centred in the SZ emission. Most of the clusters have been selected by the large displacement of the BCG with respect to SZ centre of X-ray peak/centre, while a fraction relies on a gas morphology index $A_{\rm phot}$. In the latter case, the BCG is not necessarily significantly displaced from the gas centre, as shown by SPT-CLJ0014−4952.

and σ_{ij} is the associated statistical Poisson error. We obtain $N_{ij}^{z=0}$ by correcting it by the evolutionary factor $E^2(z)$, where $E(z) = \sqrt{\Omega_m(1+z)^3 + \Omega_\Lambda}$.[8]

The errors of the stacked LF are computed as

$$\delta N_j = \frac{1}{\left(\sum_i 1/\sigma_{ij}^2\right)^{1/2}}.$$

Once the stacked binned LF is constructed, we fit for the three parameters of the Schechter function (SF) Φ^*, m^*, and α (Schechter 1976),

$$\phi(m) = 0.4\ln(10)\ \Phi^* 10^{0.4(m^*-m)(\alpha+1)} \exp(-10^{0.4(m^*-m)}).$$

4.1.3 LF robustness tests

We use the offset between the BCG and the gas centre, as well as the gas morphology, to classify the cluster dynamical state, and use the BCG as the cluster centre to study galaxy populations. If galaxy transformation takes place in clusters, as they merge and relax, evidence of such transformation should be detected even if we vary the cluster centre. To corroborate this, we run several tests on our samples. We take the relaxed and disturbed samples and randomize the cluster centre position within the 0.4-1 r_{200} range from the gas proxy, with a flat probability 600 times. In particular, we stack the LF of clusters under different configurations including (A) randomizing the cluster centre position from the X-ray peak/centroid for the relaxed sample, and (B) randomizing the cluster centre position from the SZ centroid (a loose gas centre proxy to compare to the relaxed sample) for the disturbed sample. We also include another two cases for comparison; (C) we stack the disturbed sample LF using the SZ centroid as a centre, and (D) we stack the LF of the intermediate population, using the BCG as the cluster centre. Case D is used to highlight differences between the intermediate population and the two extremes we are probing. We then create 600 stacked LF by randomly selecting N unique clusters from this sample. As the goal is to compare these randomized samples to the relaxed and disturbed samples, N corresponds to the number of clusters of the largest sample, relaxed or disturbed.

4.1.4 Halo occupation number

To estimate the richness of the clusters and compare the number of galaxies as a function of the dynamical state, we estimate the halo occupation number (HON). We estimate the HON by integrating the Schechter function.

$$N = 1 + N^s, \text{ with } N^s = V\phi^* \int_{y_{low}}^{\infty} y^\alpha e^{-y}\, dy,$$

where 1 accounts for the BCG, which is not part of the LF fit, V is the cluster virial volume, $y_{low} = L_{low}/L_*$, and α and ϕ^* are obtained by fitting the Schechter function in (Section 4.1.2). We integrate the LF to $m^* + 3$[9] to compare to the work of Lin, Mohr & Stanford (2004).

[8]This scaling is appropriate for self-similar evolution, where the characteristic density within the cluster virial region will scale with the critical density of the Universe.

[9]Notice that on average, our individual LFs depth allows us to reach $m^* + 3$ only in clusters to redshift 0.61 ± 0.04, beyond that, we are fitting shallower LFs.

5 RESULTS

5.1 Brightest cluster galaxies

5.1.1 Membership tests

BCG selection is a key component of this work. In Section 2.4, we used the spectroscopic data of 68 systems to show that we expect a miss-classification rate of about 2 per cent. This may vary with cluster sample type. For example, as the disturbed sample is defined by how far the BCG is from the SZ centroid, the likelihood of choosing a non-cluster galaxy may be higher. Here, we look into the sub-samples in more detail.

We compare our selected SPT BCGs to candidates found in McDonald et al. (2016). The selection of BCGs in McDonald et al. (2016) has been done independently from ours, but the methodology is similar. McDonald et al. (2016) selected the brightest RS galaxy within r_{200}, but then visually inspected the images to change the candidate if any of the following conditions were met: (i) if more than one dominant galaxy is found significantly closer to the X-ray peak (29 per cent of cases) or (ii) if there is a blue galaxy close to the X-ray peak (3 per cent of cases). Under those conditions we expect our disturbed sample to only contain BCGs that were not selected by the above procedure, while for the relaxed cluster sample the selection should be very similar. From 42 clusters in common between the DESY3-SPT sample and McDonald et al. (2016), we find 28 clusters in the relaxed sample and 5 in the disturbed sample. From the relaxed sample, we find five discrepancies. A visual inspection reveals that the different choice of BCGs in McDonald et al. (2016) is indeed based on those cases where there is another bright/dominant galaxy close to the X-ray centre. In all those cases (SPT-CLJ0033−6326, SPT-CLJ0232−5257, SPT-CLJ0334−4659, SPT-CLJ0533−5005, and SPT-CLJ2148−6116) our BCG selection is brighter, within 71 arcsec of the X-ray peak, while the McDonald et al. (2016) selection was even closer. From the disturbed sample we find that all the five selected BCGs are different from our selection while for the remaining nine cluster matches with the intermediate cluster sample, a match between five BCGs is found.

We also repeat the BCG background estimation done for all 288 clusters in the DESY3-SPT sample (see Section 2.4) for the disturbed sample. We find that for 23 per cent of the clusters there are no RS galaxies brighter than the BCG in the 1–3 r_{200} area. Within the same area, we find that for 34 per cent of the sample, there is only one RS galaxy brighter than the BCG. For the 23/13/7 per cent of the sample, we find 2/3/4 galaxies brighter than the BCG. Combining this information we get a probability of miss-identification of 14 per cent, the same when all 288 clusters are used. We compare our disturbed cluster sample BCGs to the RM selection. A match between clusters renders 36 matches and 7 SPT clusters with no RM counterpart. All the non-matches correspond to RM masked areas where a no cluster search was carried out. When matching the BCG, we find that out of the 36 matches, only 5 correspond to our BCG selection. For 16 cases, the RM BCGs correspond to a bright galaxy close to the SZ-centroid, while for 15 cases a different galaxy, much fainter, is chosen.

Finally, a cross-match between the spectroscopic sample and the BCGs from the disturbed cluster sample renders six matches; three selected from X-ray information (SPT-CLJ0014−4952, SPT-CLJ0212−4657, and SPT-CLJ0551−5709), and three by $D_{BCG\text{-}SZ}$ (SPT-CLJ0145−5301, SPT-CLJ0307−6225, and SPT-CLJ0403−5719). All of them at the same redshift as their host cluster. This provides confidence in our BCG selection.

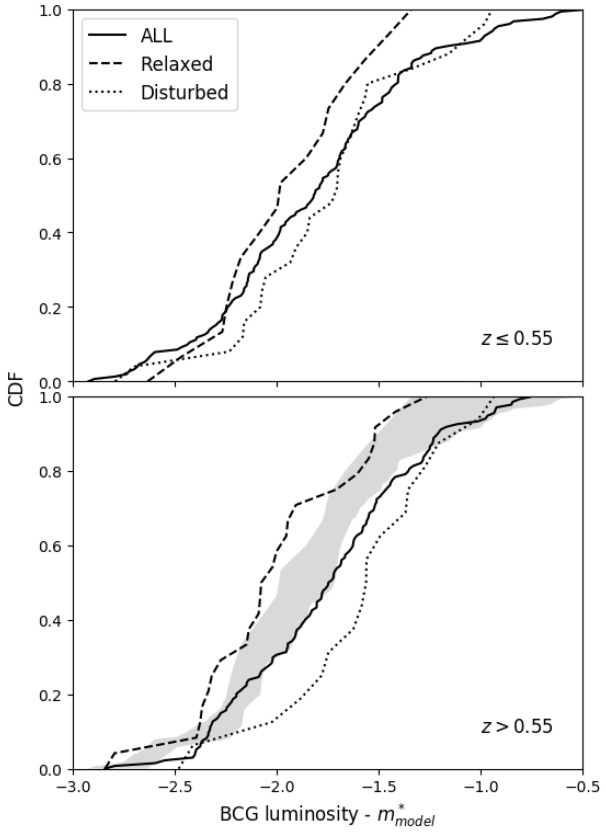

Figure 5. Cumulative distribution of the BCG luminosity (r band at $z < 0.35$, i band at $z < 0.7$, and z band at $z > 0.7$) for the total (solid line), relaxed (dashed line), and disturbed (dotted line) cluster samples. *Top panel*: BCGs at $z \leq 0.55$. *Bottom panel*: BCGs at $z > 0.55$. Shaded area corresponds to the area covered by the BCG distributions at the low-redshift bin.

5.1.2 *Brightness and colour*

The BCGs have an average luminosity of $m^* - 1.7$, with 95 per cent of the population fainter than $m^* - 2.45$, and all of them fainter than $m^* - 2.8$. We chose to limit the brightness of the BCG to $m^* - 4$, and the observed distribution supports this choice. The cumulative BCG luminosity distributions, with respect to the host cluster m^*, for the disturbed, relaxed, and for all clusters are shown in Fig. 5. The plots show that the BCG luminosity distribution of the samples agree at lower redshift (top panel), while they are somewhat different at higher redshift (bottom panel). In the high-redshift bin the BCGs in relaxed clusters are brighter than in disturbed clusters, and for all clusters combined. At $z \leq 0.55$, a Kolmogorov–Smirnov (KS) test shows that a comparison between the total and the relaxed sample renders a p-value of 0.64, while the p-value between the disturbed and relaxed sample is 0.32, confirming their agreement (or the lack of evidence of disagreement). At $z > 0.55$, the KS test renders a p-value of 0.0083 between the total and the relaxed sample, and a p-value of 0.0028 between the disturbed and relaxed sample. Both results reject the hypothesis that the distributions come from the same parent distribution. In general, there are several potential reasons for the difference in relaxed and disturbed systems. In relaxed clusters, cooling from the ICM will contribute to the BCG mass growth; if cool cores last for $\sim$10 Gyr, BCGs would gain $\gtrsim 10^{10}\,M_\odot$ from cooling even if it is highly suppressed by the AGN (see McDonald et al. 2018, and references therein). In regards to our samples, a factor to consider is that the BCG stellar mass correlates with halo mass (Brough et al. 2008; Lidman et al. 2012). As the average total mass of the relaxed sample is slightly higher than the average total mass of the disturbed clusters (see Fig. 3), one would expect BCGs in relaxed systems to be more luminous. In term of photometry, deblending problems could also bias high the luminosity of BCGs in relaxed systems as they are located in crowded places. Nevertheless, the BCG luminosity of relaxed and disturbed samples in the $z < 0.55$ range agree, indicating that such effects must be of little importance. Understanding how those elements can play a different (larger) role at $z > 0.55$ is more challenging. We can speculate that at higher redshift galaxies sink more efficiently to the bottom of the potential, merging with the BCG and increasing its luminosity. As the relevant dynamical friction time-scales depend on the distance between the BCG and other cluster galaxies, a factor to consider is the clusters size. As clusters radius are a function of the critical density of the Universe, they are more compact at higher redshifts; r_{200} for a given cluster is smaller at high redshift than at low redshift as $r_{200} \propto 1.0/(\Omega_M(1+z)^3 + \Omega_\Lambda)^{2/3}$. Having galaxies closer together at higher redshift would make dynamical friction indeed more efficient.

In the case of the disturbed sample, BCGs may suffer the loss of weakly bound stars during the merging event, although with a KS test p-value of 0.2736, we cannot reject the hypothesis that both the disturbed sample and the all clusters sample, come from the same parent distribution.

In terms of colour, we find no significant differences between the distributions above and below $z = 0.55$. For the 288 BCGs in the full DESY3-SPT sample, only 2 per cent of the BCGs are bluer than the RS (defined with a width of ± 0.22 mag; see Section 2.4). This fraction is lower than what has been reported in the literature. Based on SDSS DR6 data of over 14 300 BCGs in the 0.1–0.3 redshift range, Pipino et al. (2011) reported 4–9 per cent of the BCGs being 0.3 mag bluer than the $g - r$ RS. If we use 0.3 as a colour limit, we only find that 1 per cent of all SPT BCGs studied here are blue. This difference is alleviated if we factor in the cluster mass; indeed, when a mass cut is applied ($\gtrsim 1.4 \times 10^{14}\,M_\odot$), Pipino et al. (2011) found a lower rate of 6 per cent. Given that our systems are among the most massive clusters in the Universe, a 1 per cent rate of blue BCGs seems consistent with previous findings.

Comparing the colours of the BCGs in the relaxed and disturbed samples we find no blue BCGs in the former. The relaxed sample includes SPT-CLJ2043−5035, a cluster with excess blue emission in *HST* images and a star formation rate of $33.1^{+7.1}_{-4.6}\,M_\odot\,yr^{-1}$ (McDonald et al. 2019). Our DES photometry shows a colour of 0.17 mag bluer than the RS for SPT-CLJ2043−5035, placing the BCG colour within our 0.22 RS magnitude width, showing that the RS width also includes star-forming BCGs. In the disturbed sample, we find three blue BCGs, about 7 per cent, in the latter sample. It is worth noting that as the disturbed sample is defined by how far the BCG is from the SZ centroid, the likelihood of choosing a foreground (bluer) galaxy may be higher, although we showed in Sections 2.4 and 5.1.1 that overall with our selection we expect a miss-classification rate of about 2–9 per cent.

In our relaxed sample the well-known cool-core cluster SPT-CLJ2344–4243 (aka the Phoenix cluster McDonald et al. 2012), with a blue BCG with an extreme star formation rate, is missing. With a mass greater than $10^{15}\,M_\odot$, the Phoenix cluster is out of our mass–redshift limits. The BCGs colour distribution for the total, disturbed, and relaxed samples is shown in Fig. 6.

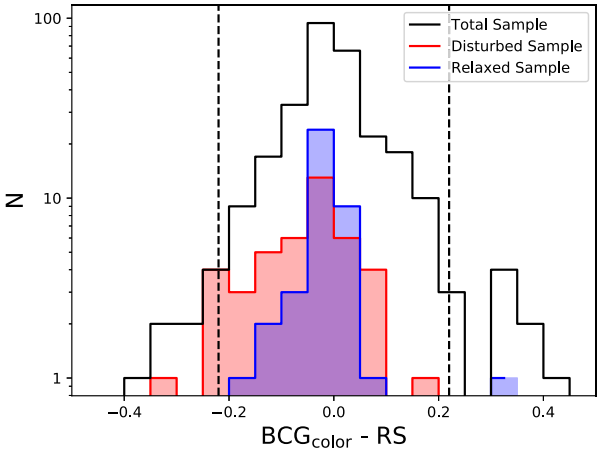

Figure 6. BCG colour for the total, the relaxed, and the disturbed cluster samples with respect to the RS (as defined in Section 2.4). The BCG colours, and m^*, are estimated depending on the cluster redshift; $g - r$ at $z < 0.35$, $r - i$ at $z < 0.7$, and $i - z$ at $z > 0.7$. Vertical lines are at ± 0.22 mag, corresponding to our 3σ RS width (López-Cruz et al. 2004).

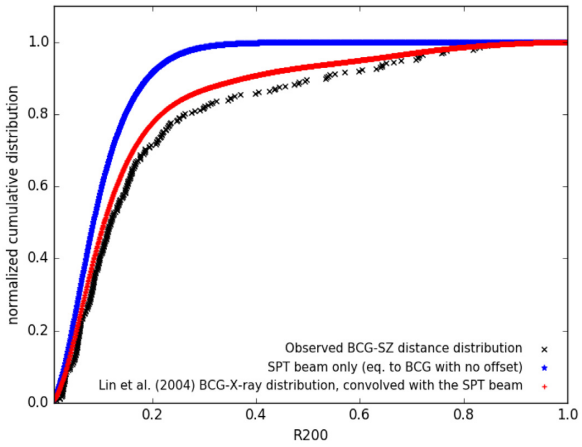

Figure 7. The full cluster sample cumulative central offset distribution (black), $D_{\rm BCG\text{-}SZ}$ compared to an X-ray sample from the literature (red), and the case of pure SPT positional uncertainty (blue).

5.1.3 BCG-SZ offset distribution

As the BCG-SZ offset distribution encodes information of the cluster sample's average dynamical state, we can compare it to other BCG clustercentric distance distributions estimated for clusters selected in a different way, and test the possibility that the SZ sample is, for example, more merger rich (Rossetti et al. 2016; Lovisari et al. 2017; Lopes et al. 2018). In particular, we compare our SZ-selected cluster sample to an X-ray selected cluster sample. An X-ray study which performs the BCG selection in a similar fashion as us (see Section 2.4) is Lin & Mohr (2004, LM04 hereafter). The LM04 sample consists of 93 galaxy clusters and groups at $z \leq 0.09$, drawn from several studies for which T_X has been measured. The cumulative offset distribution for the DESY3-SPT sample, normalized to r_{200}, and a comparison to the LM04 sample (convolved with the SPT-SZ positional uncertainty) are plotted in Fig. 7.

The blue line shows the offset distribution that would be observed if all BCGs had actually no offset from the cluster centre, because of the positional uncertainty of the SZ centroid due to the SPT beam. The black crosses show the $D_{\rm BCG\text{-}SZ}$ distribution measured in this work. The $D_{\rm BCG\text{-}SZ}$ distribution for the SPT sample studied here is consistent with LM04 results; a KS test shows a $p = 0.094$ (at D $= 0.072$ r_{200}) between the LM04 sample and our $D_{\rm BCG\text{-}SZ}$ distribution providing no evidence that SPT-SZ selected clusters are richer in disturbed clusters than the LM04 sample, a result that confirms our findings in Song et al. (2012).

The ideal comparison is between samples that cover the same redshift range with the BCGs selected in the same fashion. In the LM04 case, the X-ray sample is selected in a rather inhomogeneous way and consists of low-redshift systems. On the other hand the LM04 BCG selection is very similar to ours. X-ray studies that span larger redshift ranges and have been used to compare to SZ samples are those of HIFLUGCS (Reiprich & Böhringer 2002), REXCESS (Böhringer et al. 2007), and MACS (Ebeling, Edge & Henry 2001). In particular, Rossetti et al. (2016) showed discrepancies between the offset distribution of the Planck sample (Planck Collaboration XX 2014) and the aforementioned X-ray surveys. The difficulty with using such samples is that the BCG has been selected in an 'inhomogeneous' fashion. While Rossetti et al. (2016) highlights the differences between the Planck sample and the X-ray studies, it is also true that a comparison between some of those very same X-ray samples, e.g. HIFLUGCS versus REXCESS, will also reject the hypothesis that those two offset distributions are drawn from the same parent distribution. This is an expected outcome from samples that have a different BCG selection function.

We model the offset distribution using a sum of two distributions. One to describe a cluster population with small $D_{\rm BCG\text{-}SZ}$, and the second one to model the disturbed cluster population. Following Saro et al. (2015), we use the equation:

$$P(x) = 2\pi x \left(\frac{\rho_0}{2\pi\sigma_0^2} e^{-\frac{x^2}{2\sigma_0^2}} + \frac{1-\rho_0}{2\pi\sigma_1^2} e^{-\frac{x^2}{2\sigma_1^2}} \right), \quad (5)$$

where $x = r/r_{200}$ or $x = r/r_{500}$, ρ_0 is the fraction of the population more centrally located and with a variance of σ_0^2, while $1 - \rho_0$ corresponds to the more perturbed population, which has a variance of σ_1^2. We find that the observed $D_{\rm BCG\text{-}SZ}$ can be described as a dominant population of clusters with smaller $D_{\rm BCG\text{-}SZ}(\sigma_0\ (r_{200}/r_{500}) = 0.05 \pm 0.01/0.08 \pm 0.01)$, and a subdominant population of clusters with large $D_{\rm BCG\text{-}SZ}(\sigma_1\ (r_{200}/r_{500}) = 0.35 \pm 0.03/0.55 \pm 0.04)$. The fit for the two distributions, as well as the sum, is shown in Fig. 2. The marginalized posterior distributions for the three-parameter model can be seem in Fig. 8. In comparison to the results obtained by Saro et al. (2015), using redMaPPer selected central galaxies, we find that the parameters of the population with small $D_{\rm BCG\text{-}SZ}$ agree, within the error bars. For the disturbed population we find a larger σ_1 value than the Saro et al. (2015) result ($0.25^{+0.07}_{-0.06}$). This is expected as the redMaPPer central galaxy selection is based on the galaxy luminosity, galaxy photometric redshift, and local galaxy density (Rykoff et al. 2014), while in our case we are after the brightest cluster member. Furthermore, Hoshino et al. (2015) found that 20 per cent to 30 per cent of the RedMaPPer central galaxies are not the brightest cluster member. For this comparison we estimate the parameters in equation 5 using the $D_{\rm BCG\text{-}SZ}$ distribution as a function of r_{500}.

5.2 Luminosity function

We fit the Schechter function to the stacked LFs exploring several configurations such as centre (BCG or SZ), radius (1 or 0.5 r_{200}), and

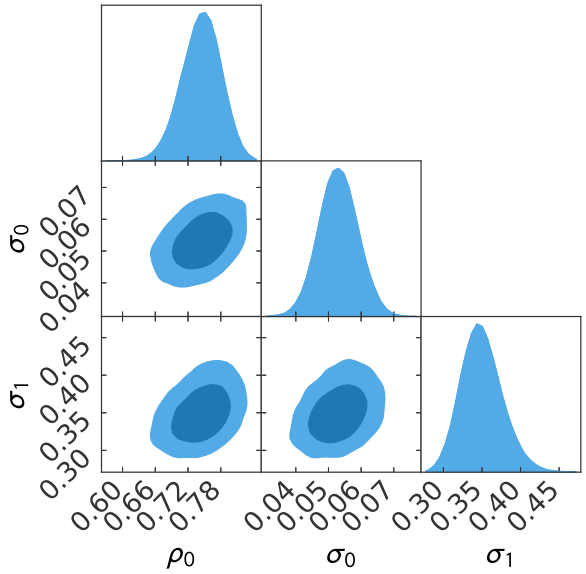

Figure 8. 1σ and 2σ solutions of the three-parameter model of equation (5) that describes the $D_{\rm BCG\text{-}SZ}$ distribution.

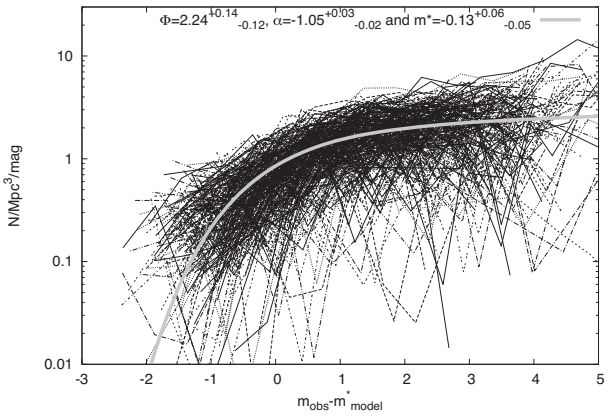

Figure 9. Luminosity functions of individual clusters for the all population up to their completeness limit. We use the m^* model and the band redwards the 4000 Å break to offset all LFs to the same photometric rest frame. The stacked result (grey solid line) is created using individual LFs up to $m^* + 3$, or the individual completeness limit if $m^* + 3$ cannot be reached.

population (all cluster galaxies included or just the RS galaxies). An example of individual LFs as well as a fit to the stacked result, for the all cluster galaxies population within r_{200}, is shown in Fig. 9 while the stacked LFs are shown for the relaxed and disturbed samples in Fig. 10. The results are summarized in Table 3 and shown in Figs 11 and 12. We discuss them in the following sub-sections.

5.2.1 *Faint-end evolution*

In general, we find differences between the faint-end slope of the relaxed and disturbed samples, as exemplified in Fig. 10. In Fig. 13, we explore the redshift evolution in the slope showing a distinct difference emerging at $z \gtrsim 0.6$, with a steeper α for the disturbed sample than for the relaxed sample. The redshift evolution figure indicates that the disturbed sample faint-end slope is consistent with no evolution, while α for the relaxed clusters seems to evolve, becoming shallow at higher redshifts. In the case of relaxed systems,

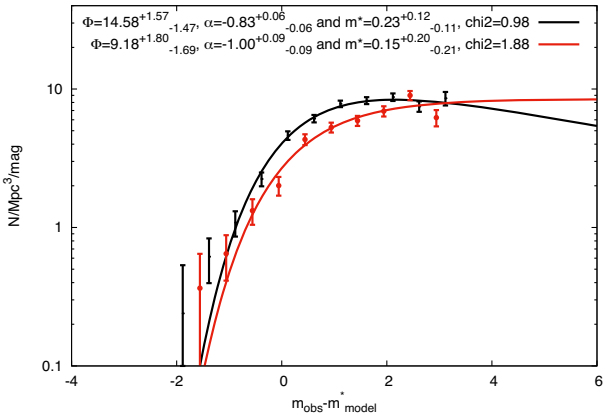

Figure 10. Stacked luminosity functions for the disturbed (red) and relaxed (black) sample, within $0.5 \times r_{200}$, including all cluster galaxies. We use the m^* model and the band redwards the 4000 Å break to offset all LFs to the same photometric frame.

the evidence for evolution is the strongest in the core of the clusters when all cluster galaxies are included (2.7σ), and the weakest at r_{200} for RS galaxies (1.0σ). All evolution results are shown in Table 4.

In the literature, only a few studies have sufficiently deep data to properly investigate the dependence (and evolution) of α on the cluster dynamical state, and all of them are at $z < 0.6$. Barrena et al. (2012) used a sample consisting of five radio-selected disturbed and five cool-core clusters at $0.2 \lesssim z \lesssim 0.3$. They find a steeper α for disturbed samples when the all cluster galaxies within r_{200} are included, but with large error bars which make them statistically indistinguishable from relaxed clusters. De Propris et al. (2013) studied a sample of 11 disturbed clusters and 5 relaxed systems at $0.2 < z < 0.6$, classified according to X-ray, strong, and weak lensing information. De Propris et al. (2013) again do not find differences between relaxed and disturbed clusters. These literature results, albeit using small samples, seem consistent with what we see at $z < 0.6$ in Fig. 13, where α agrees between samples.

To study in detail the effects of the cluster dynamical state on galaxies, we split at $z = 0.55$ the samples into two sets. The redshift cut is motivated by the fact that at around that redshift the LF parameters between the two samples start to differ, with the lower redshift bin similar to the redshift range explored by literature work, and because $z = 0.55$ is the median redshift for the B15 parent sample. The low-redshift sample results (m^* and α Schechter parameters) are shown in Fig. 11, while the high-redshift sample results are shown in Fig. 12. For both figures the solid red crosses correspond to the BCG-centred stacked LF disturbed sample results, while the blue crosses correspond to the BCG-centred stacked LF relaxed sample results. Fig. 11 shows virtually no difference between the two samples, while Fig. 12 shows the disturbed sample having a steeper faint-end slope than the relaxed sample for all the cases except for the red population within r_{200}. For the higher redshift bin, there is a tendency for disturbed and relaxed clusters to populate opposite extremes of the $m^* - \alpha$ plane, while the intermediate population (green crosses) populates the area in between the two aforementioned samples. At $z > 0.55$, this may point out to a continuous galaxy transformation as the dynamical state of the host cluster evolves, with the fainter population been accreted/destroyed as clusters relax. A higher merging rate with the central BCG may be linked to the result, found in Section 5.1.2, showing that BCGs in relaxed systems are brighter than BCGs

Table 3. Results from the Schechter luminosity function fitting using all cluster galaxies/RS alone, within a 0.5/1 R_{200} projected radius, and centred in the BCG or the SZ centroid. Also included are the fits for all the clusters excluding the disturbed and relaxed sample ('Intermediate').

Type	$z \leq 0.55$		$z > 0.55$		All redshifts		R_{200}	Pop.	Centre
	α	m^*	α	m^*	α	m^*			
All	$-1.08^{+0.03}_{-0.02}$	$-0.11^{+0.08}_{-0.07}$	$-0.90^{+0.06}_{-0.05}$	$0.08^{+0.11}_{-0.09}$	$-1.03^{+0.02}_{-0.02}$	$-0.08^{+0.06}_{-0.04}$	1	All	BCG
Intermediate	$-1.06^{+0.03}_{-0.03}$	$-0.11^{+0.10}_{-0.08}$	$-0.98^{+0.06}_{-0.05}$	$0.04^{+0.12}_{-0.12}$	$-1.05^{+0.03}_{-0.02}$	$-0.11^{+0.08}_{-0.06}$	1	All	BCG
Unrelaxed	$-1.08^{+0.07}_{-0.07}$	$0.20^{+0.19}_{-0.19}$	$-1.07^{+0.15}_{-0.13}$	$-0.06^{+0.37}_{-0.40}$	$-1.07^{+0.06}_{-0.06}$	$0.04^{+0.16}_{-0.16}$	1	All	BCG
Relaxed	$-1.03^{+0.08}_{-0.08}$	$-0.06^{+0.21}_{-0.21}$	$-0.62^{+0.11}_{-0.11}$	$0.36^{+0.16}_{-0.17}$	$-0.94^{+0.07}_{-0.05}$	$-0.05^{+0.13}_{-0.13}$	1	All	BCG
Not Gaussian	$-1.09^{+0.20}_{-0.18}$	$-0.49^{+0.58}_{-0.80}$	$-0.90^{+0.24}_{-0.19}$	$-0.11^{+0.45}_{-0.47}$	$-1.00^{+0.15}_{-0.13}$	$-0.30^{+0.36}_{-0.37}$	1	All	BCG
Gaussian	$-0.99^{+0.13}_{-0.14}$	$0.09^{+0.31}_{-0.38}$	$-0.61^{+0.12}_{-0.11}$	$0.52^{+0.17}_{-0.17}$	$-0.73^{+0.09}_{-0.08}$	$0.39^{+0.15}_{-0.14}$	1	All	BCG
All	$-0.85^{+0.04}_{-0.02}$	$0.22^{+0.05}_{-0.05}$	$-0.68^{+0.04}_{-0.04}$	$0.32^{+0.06}_{-0.06}$	$-0.81^{+0.02}_{-0.01}$	$0.24^{+0.04}_{-0.02}$	1	Red	BCG
Intermediate	$-0.84^{+0.03}_{-0.03}$	$0.22^{+0.06}_{-0.05}$	$-0.75^{+0.05}_{-0.06}$	$0.21^{+0.08}_{-0.08}$	$-0.82^{+0.03}_{-0.03}$	$0.20^{+0.05}_{-0.04}$	1	Red	BCG
Unrelaxed	$-0.85^{+0.06}_{-0.07}$	$0.18^{+0.13}_{-0.13}$	$-0.61^{+0.13}_{-0.13}$	$0.52^{+0.18}_{-0.19}$	$-0.78^{+0.07}_{-0.06}$	$0.34^{+0.12}_{-0.10}$	1	Red	BCG
Relaxed	$-0.78^{+0.08}_{-0.07}$	$0.44^{+0.14}_{-0.14}$	$-0.55^{+0.09}_{-0.09}$	$0.48^{+0.12}_{-0.12}$	$-0.70^{+0.06}_{-0.05}$	$0.34^{+0.09}_{-0.09}$	1	Red	BCG
Not Gaussian	$-1.26^{+0.18}_{-0.16}$	$-0.74^{+0.49}_{-0.78}$	$-0.34^{+0.23}_{-0.21}$	$0.82^{+0.22}_{-0.23}$	$-0.66^{+0.15}_{-0.14}$	$0.44^{+0.20}_{-0.21}$	1	Red	BCG
Gaussian	$-0.82^{+0.13}_{-0.13}$	$0.38^{+0.23}_{-0.25}$	$-0.52^{+0.09}_{-0.08}$	$0.51^{+0.11}_{-0.10}$	$-0.62^{+0.07}_{-0.05}$	$0.42^{+0.10}_{-0.08}$	1	Red	BCG
All	$-1.02^{+0.03}_{-0.03}$	$0.00^{+0.07}_{-0.06}$	$-0.95^{+0.04}_{-0.04}$	$-0.01^{+0.10}_{-0.09}$	$-1.01^{+0.03}_{-0.02}$	$-0.01^{+0.06}_{-0.04}$	1	All	SZ
Intermediate	$-0.99^{+0.03}_{-0.03}$	$0.05^{+0.09}_{-0.08}$	$-0.98^{+0.07}_{-0.06}$	$-0.06^{+0.14}_{-0.13}$	$-1.01^{+0.03}_{-0.03}$	$-0.06^{+0.07}_{-0.06}$	1	All	SZ
Unrelaxed	$-1.11^{+0.09}_{-0.07}$	$0.03^{+0.18}_{-0.19}$	$-1.17^{+0.10}_{-0.09}$	$-0.54^{+0.31}_{-0.35}$	$-1.14^{+0.06}_{-0.05}$	$-0.16^{+0.16}_{-0.17}$	1	All	SZ
Relaxed	$-1.01^{+0.08}_{-0.08}$	$0.04^{+0.19}_{-0.20}$	$-0.71^{+0.12}_{-0.11}$	$0.41^{+0.18}_{-0.19}$	$-0.93^{+0.07}_{-0.06}$	$0.08^{+0.14}_{-0.13}$	1	All	SZ
Not Gaussian	$-1.03^{+0.21}_{-0.19}$	$-0.03^{+0.47}_{-0.59}$	$-0.92^{+0.22}_{-0.19}$	$-0.16^{+0.46}_{-0.47}$	$-0.98^{+0.15}_{-0.13}$	$-0.14^{+0.33}_{-0.36}$	1	All	SZ
Gaussian	$-0.85^{+0.14}_{-0.13}$	$0.28^{+0.28}_{-0.32}$	$-0.69^{+0.10}_{-0.11}$	$0.44^{+0.16}_{-0.18}$	$-0.75^{+0.09}_{-0.07}$	$0.38^{+0.15}_{-0.13}$	1	All	SZ
All	$-0.82^{+0.03}_{-0.03}$	$0.25^{+0.05}_{-0.04}$	$-0.67^{+0.04}_{-0.04}$	$0.31^{+0.06}_{-0.06}$	$-0.79^{+0.01}_{-0.02}$	$0.24^{+0.03}_{-0.02}$	1	Red	SZ
Intermediate	$-0.80^{+0.04}_{-0.02}$	$0.28^{+0.06}_{-0.05}$	$-0.71^{+0.05}_{-0.06}$	$0.24^{+0.09}_{-0.08}$	$-0.80^{+0.03}_{-0.03}$	$0.24^{+0.05}_{-0.04}$	1	Red	SZ
Unrelaxed	$-0.87^{+0.06}_{-0.06}$	$0.16^{+0.12}_{-0.12}$	$-0.80^{+0.10}_{-0.10}$	$0.22^{+0.18}_{-0.18}$	$-0.85^{+0.06}_{-0.05}$	$0.20^{+0.11}_{-0.10}$	1	Red	SZ
Relaxed	$-0.77^{+0.08}_{-0.08}$	$0.41^{+0.14}_{-0.14}$	$-0.55^{+0.09}_{-0.08}$	$0.51^{+0.12}_{-0.12}$	$-0.69^{+0.05}_{-0.06}$	$0.35^{+0.09}_{-0.09}$	1	Red	SZ
Not Gaussian	$-1.31^{+0.17}_{-0.15}$	$-0.85^{+0.55}_{-0.85}$	$-0.51^{+0.22}_{-0.20}$	$0.59^{+0.24}_{-0.26}$	$-0.79^{+0.14}_{-0.13}$	$0.21^{+0.22}_{-0.24}$	1	Red	SZ
Gaussian	$-0.87^{+0.12}_{-0.10}$	$0.30^{+0.23}_{-0.22}$	$-0.57^{+0.08}_{-0.07}$	$0.42^{+0.11}_{-0.09}$	$-0.65^{+0.06}_{-0.06}$	$0.36^{+0.09}_{-0.09}$	1	Red	SZ
All	$-0.97^{+0.03}_{-0.01}$	$0.11^{+0.07}_{-0.04}$	$-0.80^{+0.05}_{-0.05}$	$0.26^{+0.09}_{-0.08}$	$-0.91^{+0.02}_{-0.01}$	$0.15^{+0.05}_{-0.02}$	½	All	BCG
Intermediate	$-0.94^{+0.03}_{-0.02}$	$0.15^{+0.08}_{-0.04}$	$-0.80^{+0.07}_{-0.06}$	$0.34^{+0.11}_{-0.10}$	$-0.93^{+0.02}_{-0.02}$	$0.14^{+0.06}_{-0.03}$	½	All	BCG
Unrelaxed	$-0.98^{+0.12}_{-0.10}$	$0.25^{+0.26}_{-0.28}$	$-1.10^{+0.13}_{-0.11}$	$-0.16^{+0.33}_{-0.34}$	$-1.00^{+0.09}_{-0.09}$	$0.15^{+0.20}_{-0.21}$	½	All	BCG
Relaxed	$-1.10^{+0.08}_{-0.08}$	$-0.18^{+0.22}_{-0.25}$	$-0.54^{+0.10}_{-0.11}$	$0.60^{+0.13}_{-0.14}$	$-0.83^{+0.06}_{-0.06}$	$0.23^{+0.12}_{-0.11}$	½	All	BCG
Not Gaussian	$-1.70^{+0.23}_{-0.10}$	$-8.70^{+7.49}_{-1.49}$	$-0.94^{+0.25}_{-0.23}$	$0.23^{+0.37}_{-0.47}$	$-0.96^{+0.19}_{-0.17}$	$0.10^{+0.34}_{-0.40}$	½	All	BCG
Gaussian	$-0.97^{+0.12}_{-0.12}$	$-0.04^{+0.32}_{-0.33}$	$-0.58^{+0.11}_{-0.10}$	$0.52^{+0.16}_{-0.14}$	$-0.70^{+0.09}_{-0.07}$	$0.37^{+0.13}_{-0.13}$	½	All	BCG
All	$-0.80^{+0.03}_{-0.02}$	$0.34^{+0.06}_{-0.03}$	$-0.69^{+0.04}_{-0.04}$	$0.31^{+0.07}_{-0.07}$	$-0.77^{+0.02}_{-0.02}$	$0.31^{+0.05}_{-0.03}$	½	Red	BCG
Intermediate	$-0.78^{+0.04}_{-0.02}$	$0.36^{+0.06}_{-0.04}$	$-0.73^{+0.06}_{-0.06}$	$0.15^{+0.09}_{-0.10}$	$-0.78^{+0.02}_{-0.03}$	$0.28^{+0.05}_{-0.03}$	½	Red	BCG
Unrelaxed	$-0.82^{+0.12}_{-0.12}$	$0.52^{+0.22}_{-0.23}$	$-0.74^{+0.15}_{-0.14}$	$0.48^{+0.23}_{-0.25}$	$-0.77^{+0.09}_{-0.09}$	$0.50^{+0.15}_{-0.15}$	½	Red	BCG
Relaxed	$-0.81^{+0.08}_{-0.07}$	$0.31^{+0.16}_{-0.16}$	$-0.45^{+0.10}_{-0.10}$	$0.69^{+0.13}_{-0.12}$	$-0.64^{+0.06}_{-0.06}$	$0.50^{+0.09}_{-0.09}$	½	Red	BCG
Not Gaussian	$-1.28^{+0.20}_{-0.19}$	$-0.93^{+0.64}_{-1.24}$	$-0.28^{+0.29}_{-0.27}$	$1.00^{+0.22}_{-0.25}$	$-0.65^{+0.18}_{-0.18}$	$0.62^{+0.23}_{-0.24}$	½	Red	BCG
Gaussian	$-0.78^{+0.14}_{-0.13}$	$0.37^{+0.25}_{-0.26}$	$-0.49^{+0.10}_{-0.09}$	$0.51^{+0.13}_{-0.12}$	$-0.54^{+0.08}_{-0.07}$	$0.46^{+0.10}_{-0.10}$	½	Red	BCG
All	$-0.94^{+0.03}_{-0.01}$	$0.18^{+0.07}_{-0.03}$	$-0.84^{+0.05}_{-0.05}$	$0.25^{+0.09}_{-0.09}$	$-0.91^{+0.02}_{-0.01}$	$0.18^{+0.04}_{-0.02}$	½	All	SZ
Intermediate	$-0.95^{+0.04}_{-0.01}$	$0.13^{+0.07}_{-0.04}$	$-0.91^{+0.06}_{-0.06}$	$0.18^{+0.12}_{-0.12}$	$-0.95^{+0.02}_{-0.02}$	$0.11^{+0.06}_{-0.03}$	½	All	SZ
Unrelaxed	$-0.75^{+0.08}_{-0.08}$	$0.65^{+0.15}_{-0.14}$	$-0.73^{+0.14}_{-0.13}$	$0.48^{+0.22}_{-0.25}$	$-0.77^{+0.08}_{-0.08}$	$0.60^{+0.14}_{-0.13}$	½	All	SZ
Relaxed	$-1.03^{+0.08}_{-0.08}$	$-0.13^{+0.20}_{-0.20}$	$-0.69^{+0.10}_{-0.09}$	$0.45^{+0.15}_{-0.15}$	$-0.85^{+0.06}_{-0.06}$	$0.22^{+0.11}_{-0.11}$	½	All	SZ
Not Gaussian	$-1.32^{+0.23}_{-0.21}$	$-0.73^{+0.56}_{-0.86}$	$-0.84^{+0.27}_{-0.25}$	$0.27^{+0.39}_{-0.53}$	$-0.80^{+0.18}_{-0.15}$	$0.24^{+0.27}_{-0.29}$	½	All	SZ
Gaussian	$-0.97^{+0.12}_{-0.10}$	$-0.03^{+0.32}_{-0.31}$	$-0.54^{+0.12}_{-0.11}$	$0.75^{+0.15}_{-0.15}$	$-0.64^{+0.09}_{-0.08}$	$0.59^{+0.14}_{-0.13}$	½	All	SZ
All	$-0.79^{+0.02}_{-0.02}$	$0.36^{+0.05}_{-0.03}$	$-0.62^{+0.05}_{-0.04}$	$0.43^{+0.08}_{-0.06}$	$-0.71^{+0.01}_{-0.02}$	$0.42^{+0.03}_{-0.02}$	½	Red	SZ
Intermediate	$-0.78^{+0.03}_{-0.03}$	$0.36^{+0.06}_{-0.04}$	$-0.70^{+0.06}_{-0.06}$	$0.25^{+0.10}_{-0.09}$	$-0.78^{+0.03}_{-0.01}$	$0.31^{+0.05}_{-0.03}$	½	Red	SZ
Unrelaxed	$-0.76^{+0.07}_{-0.06}$	$0.42^{+0.12}_{-0.12}$	$-0.43^{+0.14}_{-0.13}$	$0.84^{+0.16}_{-0.16}$	$-0.63^{+0.08}_{-0.06}$	$0.68^{+0.11}_{-0.09}$	½	Red	SZ
Relaxed	$-0.76^{+0.08}_{-0.08}$	$0.35^{+0.16}_{-0.15}$	$-0.36^{+0.11}_{-0.09}$	$0.86^{+0.12}_{-0.11}$	$-0.62^{+0.06}_{-0.06}$	$0.57^{+0.10}_{-0.09}$	½	Red	SZ
Not Gaussian	$-1.07^{+0.23}_{-0.21}$	$-0.30^{+0.53}_{-0.76}$	$-0.39^{+0.27}_{-0.25}$	$0.94^{+0.23}_{-0.25}$	$-0.58^{+0.19}_{-0.18}$	$0.78^{+0.21}_{-0.24}$	½	Red	SZ
Gaussian	$-0.78^{+0.13}_{-0.11}$	$0.43^{+0.22}_{-0.22}$	$-0.44^{+0.10}_{-0.09}$	$0.59^{+0.12}_{-0.12}$	$-0.53^{+0.07}_{-0.07}$	$0.48^{+0.10}_{-0.09}$	½	Red	SZ

Table 4. Result from a linear fit to the data separate in five redshift bins. The centre used is the BCG.

Sample	Intercept	Slope	Significance	R/R_{200}	Gal. type[a]
All	$-1.24^{+0.11}_{-0.12}$	$0.46^{+0.24}_{-0.24}$	1.92	1	All
Intermediate	$-1.22^{+0.12}_{-0.13}$	$0.36^{+0.26}_{-0.27}$	1.33	1	All
Unrelaxed	$-0.82^{+0.35}_{-0.35}$	$-0.37^{+0.70}_{-0.70}$	0.53	1	All
Relaxed	$-1.53^{+0.34}_{-0.33}$	$1.27^{+0.64}_{-0.65}$	1.95	1	All
All	$-1.04^{+0.12}_{-0.12}$	$0.54^{+0.25}_{-0.25}$	2.16	1	Red
Intermediate	$-0.96^{+0.14}_{-0.15}$	$0.38^{+0.31}_{-0.31}$	1.23	1	Red
Unrelaxed	$-0.78^{+0.37}_{-0.38}$	$-0.05^{+0.77}_{-0.76}$	0.06	1	Red
Relaxed	$-1.03^{+0.32}_{-0.33}$	$0.64^{+0.62}_{-0.63}$	1.02	1	Red
All	$-1.12^{+0.13}_{-0.12}$	$0.48^{+0.26}_{-0.26}$	1.85	1/2	All
Intermediate	$-1.17^{+0.14}_{-0.13}$	$0.50^{+0.30}_{-0.29}$	1.72	1/2	All
Unrelaxed	$-0.46^{+0.48}_{-0.48}$	$-1.19^{+0.91}_{-0.90}$	1.31	1/2	All
Relaxed	$-1.86^{+0.36}_{-0.37}$	$1.98^{+0.73}_{-0.73}$	2.71	1/2	All
All	$-0.95^{+0.14}_{-0.14}$	$0.50^{+0.29}_{-0.30}$	1.67	1/2	Red
Intermediate	$-0.78^{+0.16}_{-0.16}$	$0.16^{+0.34}_{-0.35}$	0.46	1/2	Red
Unrelaxed	$-0.70^{+0.54}_{-0.53}$	$-0.46^{+1.05}_{-1.05}$	0.44	1/2	Red
Relaxed	$-1.47^{+0.38}_{-0.39}$	$1.62^{+0.78}_{-0.78}$	2.08	1/2	Red

[a] 'All' corresponds to all cluster galaxies, while 'red' corresponds to RS galaxies.

in disturbed clusters as well as BCGs from the total 288 clusters sample.

The difference between the lower and higher redshift samples might imply a larger galaxy merger rate, or galaxy destruction at higher redshift. Studies measuring the galaxy merger rate in clusters seem to indicate a higher rate at high redshift than in the field. van Dokkum et al. (1999) used *HST* imaging of the massive cluster MS 1054−03 at $z = 0.83$ to show a higher merger rate for galaxies in this cluster in comparison to the field. In terms of the dynamical state of MS 1054−03, Tran et al. (1999) conclude from the agreement between multiple mass proxies (dynamical, X-ray, and weak lensing) that it is a relaxed cluster, in spite of the irregular morphology of its galaxy distribution. Similar results have been found at even higher redshifts (e.g. Lotz et al. 2013; Watson et al. 2019) but such studies have been limited to the bright end of the LF. To explain the change of the shape of the LF, the efficiency of merging or destroying sub-L^* galaxies must be higher at higher redshift. Some hint of this can be found in studies dedicated to exploring the population of galaxies that contribute to the assembly of BCGs through cosmic time. Burke & Collins (2013) explored the inner 50 kpc radius at redshift 0.8–1.3. They counted all galaxies up to 3.25 mag fainter than the BCG, which corresponds in average to a depth of $m^* + 1.55$ for our BCG luminosity distribution, and found a larger number of large BCG companions than small galaxies companions. Similar results were found by Lidman et al. (2013) on a sample of 19 clusters at $0.84 < z < 1.46$. Lidman et al. (2013) found an excess of bright companions (second to fourth brightest cluster members) within the 70 kpc inner annuli. At $0.15 < z < 0.40$, exploring a distance between 30 and 50 kpc from the BCG, Edwards & Patton (2012) found the opposite, a larger number of 1:10 and 1:20 BCG companions. Although this may be what we are seeing, the radius we can resolve is about 10–20 times larger, and from dynamical friction arguments, galaxies at distances larger than ∼200 kpc, may take longer than the Hubble time to merge with the BCG (Burke & Collins 2013). Interestingly, Bîrzan et al. (2017) arrived at a similar conclusion (an increase of galaxy minor mergers at high redshift) by studying the radio luminosity evolution of BCGs (or central radio sources) in SPT clusters. To power the highest luminosity sources at $z > 0.6$, a higher merging rate of gas-rich galaxies with the BCG may be required.

A low-redshift study that investigated the LF slope as a function of the cluster dynamical state is that of Ribeiro et al. (2013, R13 hereafter). R13 studied a sample of 183 clusters at $z \leq 0.1$, classifying them as relaxed (84 per cent) or disturbed (16 per cent) according to the Gaussian or non-Gaussian shape of the line-of-sight galaxy velocity distribution. They found a steeper LF faint end for relaxed clusters. As mentioned previously, if we use the lower redshift sample, closer to the range that R13 probes, we find α is consistent between the disturbed and relaxed samples (Figs 13 and 11). To test if the dynamical state proxy may play a role, we use 42 SPT clusters with spectroscopy from Capasso et al. (2019) and Bayliss et al. (2016), and classify their galaxy velocity distribution as Gaussian (33 clusters at $0.30 < z < 0.77$) or non-Gaussian (9 clusters at $0.48 < z < 0.75$) using the Anderson–Darling test. Stacking the LFs of the spectroscopically classified samples shows a steeper α for disturbed clusters, although with larger error bars. Results are shown in Table 3.

5.2.2 m* *evolution*

Using the BCG as the cluster centre, we find that m^* is consistent across the samples for all cases in the lower redshift bin. For the higher redshift bin, there is a tendency for the disturbed samples to have a brighter m^* than for the relaxed case, which is more significant when all cluster galaxies are used. The fainter m^* in relaxed clusters can be understood as the result of the merging of bright satellites with the BCGs as the cluster relaxes, changing the shape of the LF bright end. Such a picture is consistent with brighter and more massive BCGs in relaxed clusters as discussed in Section 5.1.2.

Literature works on $z < 0.6$ samples, such as Barrena et al. (2012) and De Propris et al. (2013), show that the m^* of relaxed and disturbed sample are in agreement across populations and radii, while works such as R13 ($z \leq 0.1$) and Wen & Han (2015) find contradictory results. Wen & Han (2015) used an optically selected cluster sample of 2092 systems (Wen & Han 2013), at $0.05 < z < 0.42$, and they used the galaxy distribution of galaxies to classify the dynamical state of the clusters. Wen & Han (2015) used r_{500} and r_{200} for the radius, the BCG for the cluster centre, and galaxies with photometric redshifts within 0.04 of the cluster redshift. They found that m^* is 0.27 mag brighter for the disturbed sample, an effect that is most important within r_{500}, with no contribution in the area between r_{500} and r_{200}. On the other hand, R13 found that relaxed clusters have a brighter m^* than the disturbed sample. A difference between R13, Wen & Han (2015) and other studies (including ours) is the dynamical state proxy. While the relaxed systems in Barrena et al. (2012) and De Propris et al. (2013) are classified using gas proxies, Wen & Han (2015) and R13 are classified using the shape of the galaxy distribution or the shape of the velocity dispersion, respectively. Different proxies may work best at different merger states and can be prone to different merger geometry. Our method is prone to select mergers in the plane of the sky, selection based on the deviation from a Gaussian shape of velocity dispersion are better at identifying mergers along the line of sight. In principle, a combination of effects could conspire to produce different results. We will explore this aspect in future work.

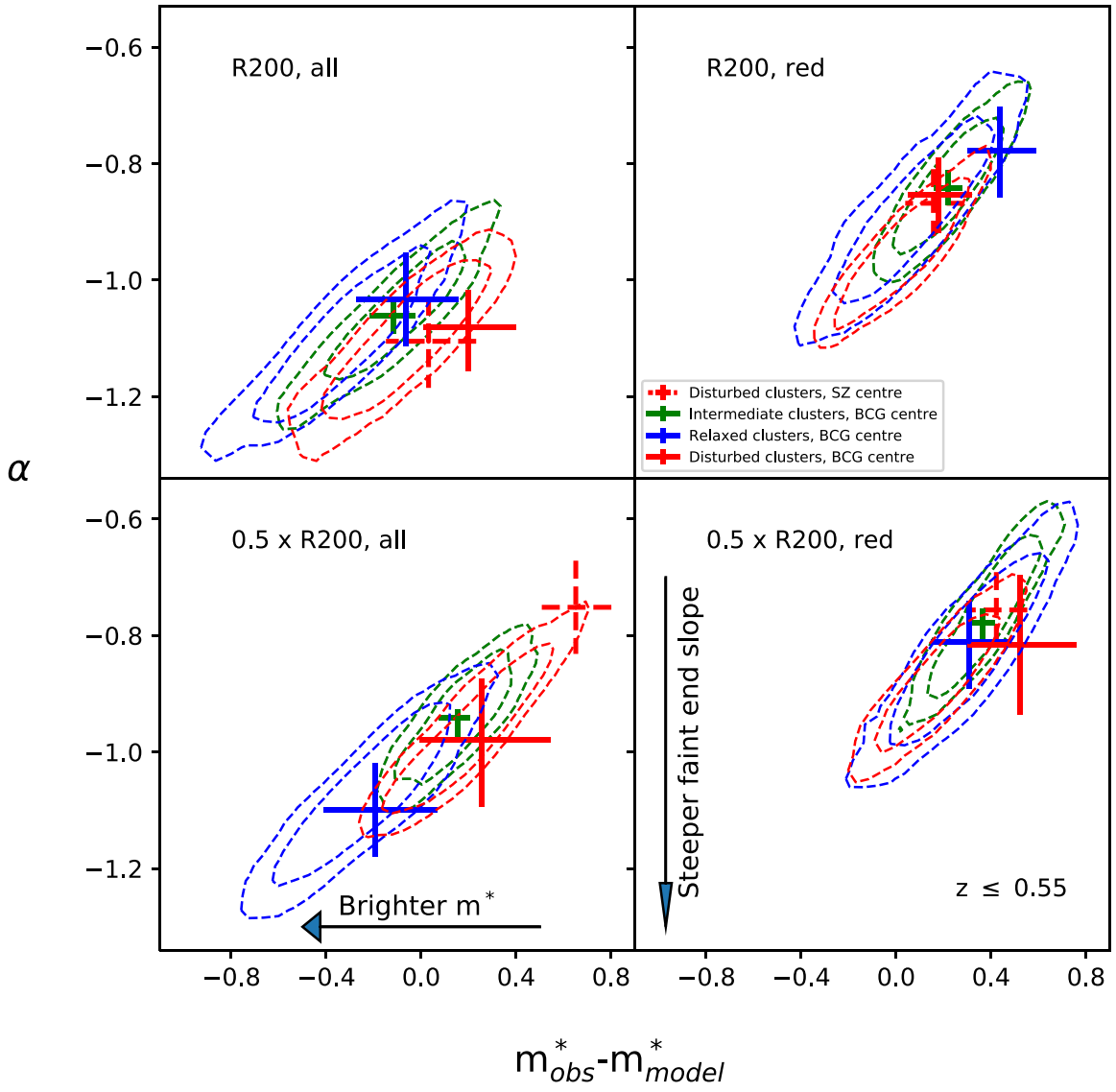

Figure 11. $\alpha - \Delta m^*(m^*_{\rm obs} - m^*_{\rm model})$ for cluster galaxies (all) and RS galaxies (red), within 1 and 0.5 r_{200}, at $z \leq 0.55$. We obtain $m^*_{\rm obs}$ by fitting the data, while $m^*_{\rm model}$ corresponds to the model as discussed in Section 2.4. Solid red crosses represent disturbed clusters using the BCG as a centre (26 clusters), dash red crosses represent disturbed clusters using the SZ centroid as a centre, blue crosses correspond to the relaxed sample (16 clusters) while green crosses correspond to the intermediate sample (see Section 4.1.3 for details; 111 clusters), both using the BCG as a centre. Dashed red/blue contours correspond to 68 per cent and 90 per cent of the fits, when the centre is randomized 600 times within 0.4–1 r_{200} of the SZ centre, for the disturbed/relaxed sample. Green contours correspond to 68 per cent and 90 per cent of the fits, obtained by stacking 26 randomly selected clusters from the intermediate cluster sample, using the BCG as a centre 600 times. At this redshift range all cluster populations seems to occupy a very similar $\alpha - \Delta m^*$ parameter space.

5.2.3 Robustness of the LF results

The robustness results are represented as dashed curves in Figs 11 and 12. While for the sample at $z < 0.55$ all curves agree, differences arise in the higher redshift range. For the $z > 0.55$ bin, Fig. 12, the relaxed sample with a randomized centre (case A; in blue) shows that, as expected, as we move away from the cluster core, more faint galaxies are included in the LF, i.e. we retrieve a steeper faint-end slope. The 68 per cent and 90 per cent intervals shown in Fig. 12 overlap partially with the LF of the disturbed sample that uses the BCG as the centre (solid red crosses). This result alone implies that we cannot rule out, at a statistically significant level, the possibility that the disturbed sample can be described as the relaxed sample with a perturbed centre, instead of a family of clusters with transformed galaxy population due to the merging process.

To further explore differences between the relaxed and disturbed samples, we randomize the centre of the disturbed sample in the same fashion (case B; red contours in Fig. 12). The distribution of case A solutions tend to occupy a different region in the α and m^* plane, than for case B, supporting the case that differences in galaxies can be found in clusters with different dynamical states, most significantly when all galaxies are considered.

If the SZ centre is used to stack the LF for disturbed clusters (case C; dashed red cross), we observe a behaviour somewhere between the disturbed and relaxed populations.

As a further comparison, we examine the intermediate population. Shown in green in Figs 11 and 12 is case D, where we draw 26/25 clusters without repetition from the low-z/high-z intermediate population, using the BCG as the cluster centre, and creating stacked

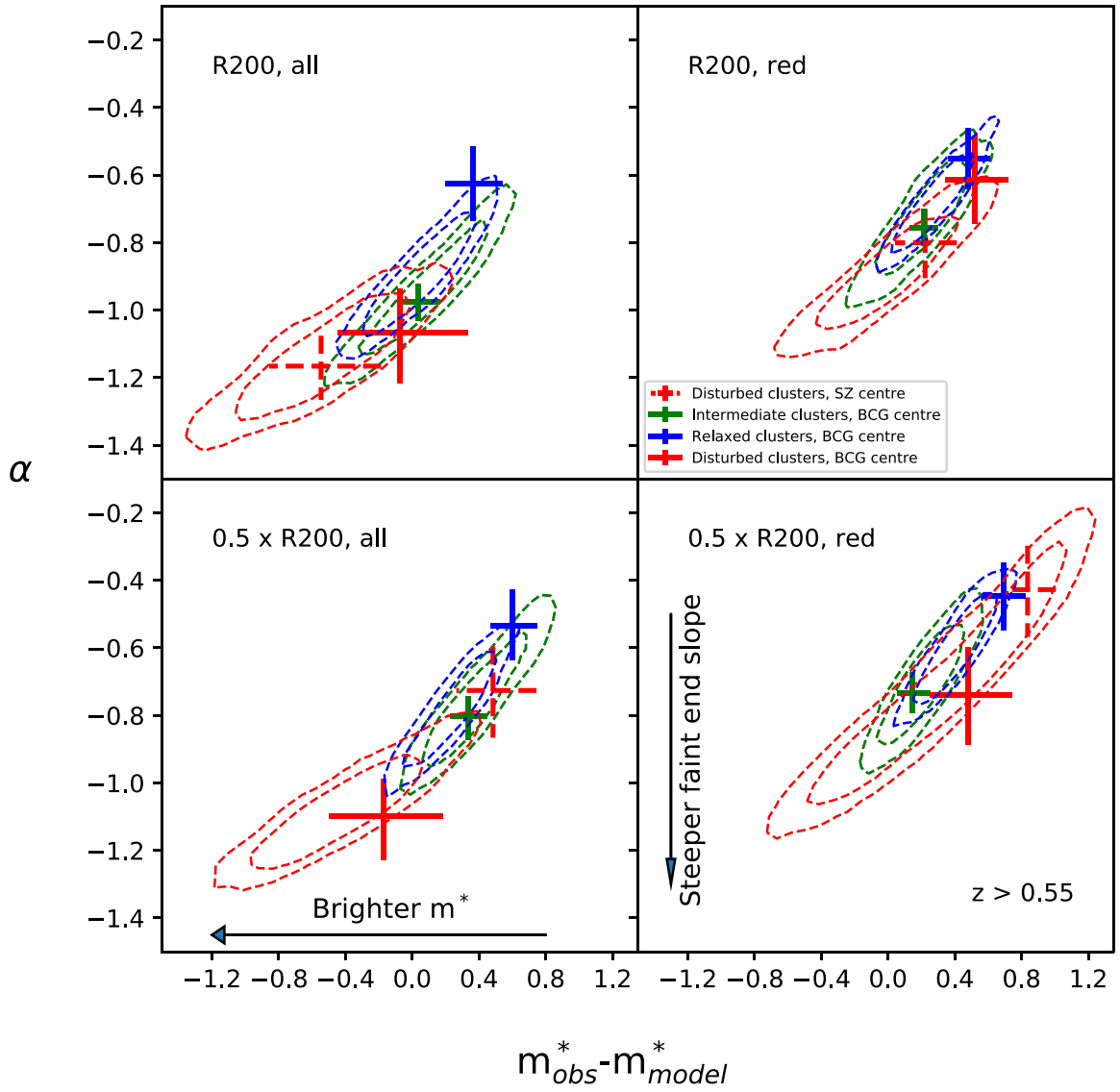

Figure 12. Similar to Fig. 11 but for $z > 0.55$. The number of disturbed clusters in this redshift bin is 17, while we find 25 relaxed systems and 93 clusters for the intermediate sample. The green curves correspond to stacking of 25 systems instead of 26, as in the $z \leq 0.55$ bin. In this redshift bin there is a tendency for the population in disturbed clusters to have a steeper α and a brighter m^*.

LFs. Compared to the disturbed and relaxed samples, they tend to populate areas in between the relaxed and disturbed BCG-centred results. This is again expected if disturbed and relaxed clusters are two extremes of the average population.

All these results combined illustrate a picture that supports a continuous galaxy transformation as clusters merge and relax. We highlight that this description is more significant when all galaxies are considered. For RS galaxies, it seems that this population is rather impervious to the cluster dynamical state, at least within the redshift and mass range, and for the number of clusters here probed.

5.2.4 Halo occupation number

The difference in the faint-end slope of the LF found between the disturbed and relaxed cluster populations indicates that a transformation is at play as clusters evolve. To measure the impact of this change on the number of galaxies, we estimate the HON for the different samples. We have integrated the LF to $m^*_{\rm model} + 3$ for the entire sample, and for the relaxed and disturbed samples to within 1 and 0.5 r_{200} for all cluster galaxies and RS galaxy only, within the whole redshift range. We use the individual cluster HON results, obtained by fixing m^* to a model and fitting for α and ϕ, the normalization of the HON versus mass relation, while keeping the slope fixed at $\gamma = 0.87$ (Lin et al. 2004). We find a normalization $N = 32.4^{+1.5}_{-2.2}$ for all clusters, lower but consistent with the value found by Lin et al. (2004) for X-ray clusters at 36 ± 9. The disturbed sample has a normalization of $32.4^{+5.7}_{-4.8}$, while the relaxed one has 31.6 ± 4.7. In the case of 0.5 r_{200}, we find $17.0^{+1.6}_{-1.1}$, $16.2^{+5.2}_{-4.2}$, and $17.4^{+3.5}_{-2.9}$ for the entire cluster sample, and for the disturbed and relaxed clusters, respectively. For the RS galaxies we found normalizations for 1/0.5 r_{200} of $24.0^{+1.7}_{-1.6}/13.5^{+1.7}_{-1.2}$, $23.4^{+4.7}_{-3.1}/12.3^{+5.5}_{-3.6}$, and $24.0^{+4.2}_{-3.6}/13.5^{+3.5}_{-2.8}$ for the entire cluster sample, and for the disturbed and relaxed clusters, respectively. All errors quoted are at the 3σ level. Above results shows that, with the current samples, and photometric depth, we are unable to constrain the HON with enough precision to find further evidence of the impact of the cluster dynamical state on the cluster's galaxies.

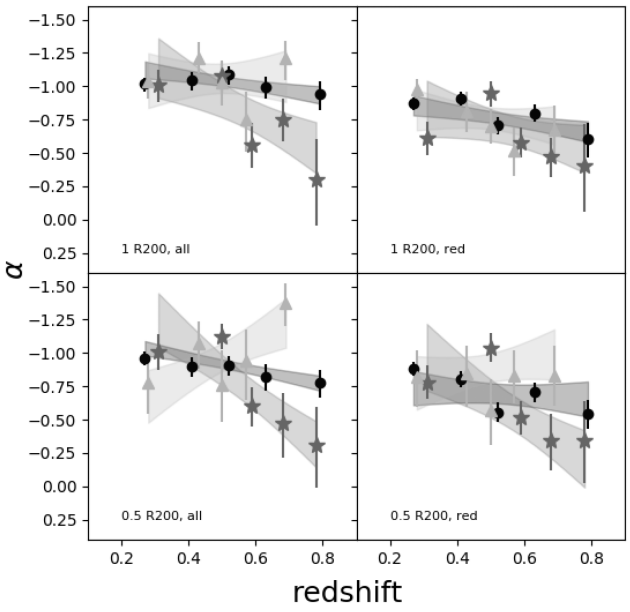

Figure 13. Faint-end α evolution for the disturbed sample (triangles), the relaxed sample (stars), and all clusters excluding the disturbed and relaxed sample (dots). The shaded areas correspond to 1σ contours.

6 CONCLUSIONS

We have used imaging from the first three years of DES to find the BCGs, within r_{200} of the centres of 288 SPT SZ-selected clusters. We have examined the offsets between the SPT-SZ centroid position and the BCG. Our findings show that we cannot reject the hypothesis that the SZ-selected radial offset distribution is similar to that seen in an X-ray-selected cluster sample at low-z, provided the BCG is selected in the same fashion. Our findings confirm the results in Song et al. (2012) providing no evidence that SPT SZ-selected cluster samples include a significantly higher fraction of mergers than X-ray-selected cluster samples. We also showed that a key condition for this comparison to be meaningful is a sample of BCGs selected in the same manner. To characterize the BCG-SZ offsets of the relaxed and disturbed clusters, we modelled the offset distribution as a sum of two distributions. We found that the $D_{\rm BCG\text{-}SZ}$ distribution with small offsets agrees with the distribution shown in Saro et al. (2015), based on redMaPPer selected central galaxies, while we find that the subdominant population of large $D_{\rm BCG\text{-}SZ}$ offsets is larger in our sample. This is expected, as the only constraint on our BCG selection is for it to be the brightest within r_{200}, while the selection of redMaPPer central galaxies is more complex. In fact, Hoshino et al. (2015) reported that 20–30 per cent of the redMaPPer central galaxies are not the brightest cluster member, which is consistent with our results.

To select the most disturbed systems we use three proxies, finding 43 clusters: the distance between the BCG and the SZ centroid $D_{\rm BCG\text{-}SZ}$, the distance between the BCG and the X-ray centroid/peak $D_{\rm BCG\text{-}X}$, and a X-ray morphology index $A_{\rm phot}$. Within a similar redshift and mass range, we also use three proxies to select the most relaxed systems: XVP cool-core clusters, and clusters with low $D_{\rm BCG\text{-}X}$ and $A_{\rm phot}$. We have found 41 relaxed clusters. We compare the galaxy populations in these two extreme dynamical states. We have built the stacked LF for all cluster galaxies and, separately, the RS galaxies, within 0.5 r_{200} and r_{200}, using the BCG as a proxy for the centre. We find that the LF of disturbed clusters have a steeper faint-end slope α and brighter m^* than the LF of relaxed clusters, although errors are large (see Table 3).

We explored the redshift evolution of α and m^*, dividing the different samples into five redshift bins (Fig. 13). We find that most of the difference between the disturbed and relaxed clusters comes from the clusters at $z \gtrsim 0.6$. To explore the effects of the observed evolutionary trends in α and m^*, as well as on the BCG, we separated the samples into two redshift bins at $z = 0.55$. The low-redshift bin (Fig. 11) shows no discernible difference between the disturbed, relaxed, and the intermediate clusters. On clusters in the high-redshift bin (Fig. 12), clear differences can be seen between the disturbed and relaxed clusters when all galaxies are used. The difference between the galaxy population in relaxed and disturbed samples is less clear for the RS population. This is confirmed by tests we use to assess the robustness of our results to the cluster centre. A possible explanation is that galaxies are accreted more efficiently at $z > 0.55$ by the BCG, as the host cluster dynamically relaxes. This would explain the shallower α, the fainter m^*, and the brighter BCGs in relaxed clusters seen in Fig. 5. Fig. 5 shows the BCG cumulative brightness distribution for the relaxed, disturbed, and intermediate cluster samples for $z \leq 0.55$ and $z > 0.55$, showing that although there is an agreement at lower redshift, BCGs in relaxed clusters in the high-redshift bin are brighter.

Previous work on the study of the LF as a function of the cluster dynamical state has only been done at $z \lesssim 0.6$. At that redshift range, our work shows agreement on the Schechter parameters between the relaxed and disturbed clusters. When compared to literature work, the largest discrepancy comes from a study on cluster samples built using the velocity distribution as the dynamical state proxy. To understand such differences we explore the velocity dispersion method over the 42 clusters in this sample with Gemini/GMOS and VLT/FORS2 spectroscopy. We use the Anderson–Darling test to classify the cluster dynamical state, finding 33 relaxed and 9 disturbed clusters. We found that the disturbed stacked LF shows a steeper faint end than the relaxed stacked LF, albeit with large error bars. We will explore this further with recently acquired Gemini/GMOS spectroscopic data for 14 disturbed clusters from this paper.

We also examined the HON to explore the effect of the dynamical state of the clusters on the number of galaxies, per cluster mass. We find an agreement within 3σ between the total, relaxed and the disturbed clusters, but with large error bars for the latter two samples. If we investigate the HON redshift evolution, with the current sample size, we find no evidence of evolution for the relaxed and disturbed clusters. A larger sample is required to investigate this aspect.

A potential source of error is the survey depth. As DES is a survey with fixed exposure times, high-redshift clusters have the faint end of the LF undersampled in comparison to the low-redshift sample. This feature translates to larger errors in α. Also, the errors in colour of the RS selected galaxies become comparable to the RS (fixed) width; at redshift $\sim$0.75/0.9 the distribution of 68/50 per cent of the sub-L^* galaxies, in the disturbed and relaxed clusters, have errors of $\sim$0.22 or less. The increasing RS scatter as a function of magnitude potentially places faint galaxies out of the RS, producing an artificially shallower α. While this may explain what we see in the relaxed sample, it does not explain the nearly constant α for the disturbed sample. Furthermore, if this effect would be a driving factor, we would expect a much stronger signal when RS galaxies are used than when all cluster galaxies are used, which is not seen. On the other hand, if the shallower α in relaxed systems is a real effect and not a product of faint photometry, then the

missing sub-L^* galaxy population must be being destroyed or going elsewhere, one of obvious candidates being the central galaxy. As we mentioned above, the BCG luminosity at $z > 0.55$ in relaxed systems are indeed brighter than BCGs in the disturbed and the intermediate clusters. Furthermore, at >1 mag brighter than the 10σ depth across the cluster fields, BCG photometry is unaffected by the survey photometric limits.

In a follow-up paper, we will expand this work using deeper *iz* data from DES Y6, as well as dedicated pointed observations of $z > 0.7$ clusters. Furthermore, in the near future, eROSITA will not only provide confirmation of the dynamical state of these clusters, but will render a sample of thousands of clusters that will allow us to test to a higher significance the findings shown here, when combined with a BCG selection in a systematic way.

ACKNOWLEDGEMENTS

TJ is pleased to acknowledge funding support from Department of Energy DE-SC0010107. AS is supported by the European Research Council (ERC)-StG 'ClustersXCosmo' grant agreement 716762, and by the Framework per l'Attrazione e il Rafforzamento delle Eccellenze per la ricerca in Italia - Ministero dell'Istruzione, dell'Università e della Ricerca (FARE-MIUR) grant 'ClustersXEuclid' R165SBKTMA. AZ is grateful of BB help and support.

Funding for the DES Projects has been provided by the U.S. Department of Energy, the U.S. National Science Foundation, the Ministry of Science and Education of Spain, the Science and Technology Facilities Council of the United Kingdom, the Higher Education Funding Council for England, the National Center for Supercomputing Applications at the University of Illinois at Urbana-Champaign, the Kavli Institute of Cosmological Physics at the University of Chicago, the Center for Cosmology and Astro-Particle Physics at the Ohio State University, the Mitchell Institute for Fundamental Physics and Astronomy at Texas A&M University, Financiadora de Estudos e Projetos, Fundação Carlos Chagas Filho de Amparo à Pesquisa do Estado do Rio de Janeiro, Conselho Nacional de Desenvolvimento Científico e Tecnológico and the Ministério da Ciência, Tecnologia e Inovação, the Deutsche Forschungsgemeinschaft and the Collaborating Institutions in the Dark Energy Survey. The Collaborating Institutions are Argonne National Laboratory, the University of California at Santa Cruz, the University of Cambridge, Centro de Investigaciones Energéticas, Medioambientales y Tecnológicas-Madrid, the University of Chicago, University College London, the DES-Brazil Consortium, the University of Edinburgh, the Eidgenössische Technische Hochschule (ETH) Zürich, Fermi National Accelerator Laboratory, the University of Illinois at Urbana-Champaign, the Institut de Ciéncies de l'Espai (IEEC/CSIC), the Institut de Física d'Altes Energies, Lawrence Berkeley National Laboratory, the Ludwig-Maximilians Universität München and the associated Excellence Cluster Universe, the University of Michigan, the National Optical Astronomy Observatory, the University of Nottingham, The Ohio State University, the University of Pennsylvania, the University of Portsmouth, SLAC National Accelerator Laboratory, Stanford University, the University of Sussex, Texas A&M University, and the OzDES Membership Consortium. This study is based in part on observations at Cerro Tololo Inter-American Observatory, National Optical Astronomy Observatory, which is operated by the Association of Universities for Research in Astronomy (AURA) under a cooperative agreement with the National Science Foundation. The DES data management system is supported by the National Science Foundation under Grant Numbers AST-1138766 and AST-1536171. The DES participants from Spanish institutions are partially supported by the Ministry of Economy and Competitiveness (MINECO) under grants AYA2015-71825, ESP2015-66861, FPA2015-68048, SEV-2016-0588, SEV-2016-0597, and MDM-2015-0509, some of which include ERDF funds from the European Union. IFAE is partially funded by the CERCA program of the Generalitat de Catalunya. Research leading to these results has received funding from the ERC under the European Union's Seventh Framework Program (FP7/2007-2013) including ERC grant agreements 240672, 291329, and 306478. We acknowledge support from the Australian Research Council Centre of Excellence for All-sky Astrophysics (CAASTRO), through project number CE110001020. This manuscript has been authored by Fermi Research Alliance, LLC under Contract No. DE-AC02-07CH11359 with the U.S. Department of Energy, Office of Science, Office of High Energy Physics. The United States Government retains and the publisher, by accepting the article for publication, acknowledges that the United States Government retains a non-exclusive, paid-up, irrevocable, world-wide license to publish or reproduce the published form of this manuscript, or allow others to do so, for United States Government purposes.

REFERENCES

Abbott T. M. C. et al., 2018, ApJS, 239, 18
Acebron A. et al., 2019, ApJ, 874, 132
Barrena R., Girardi M., Boschin W., Mardirossian F., 2012, A&A, 540, A90
Bayliss M. B. et al., 2014, ApJ, 794, 12
Bayliss M. B. et al., 2016, ApJS, 227, 3
Bîrzan L., Rafferty D. A., Brüggen M., Intema H. T., 2017, MNRAS, 471, 1766
Blasi P., Gabici S., Brunetti G., 2007, Int. J. Mod. Phys. A, 22, 681
Bleem L. E., Stalder B., Brodwin M., Busha M. T., Gladders M. D., High F. W., Rest A., Wechsler R. H., 2015, ApJS, 216, 20 (B15)
Bocquet S. et al., 2015, ApJ, 799, 214
Böhringer H. et al., 2007, A&A, 469, 363
Böhringer H. et al., 2010, A&A, 514, A32
Brimioulle F., Lerchster M., Seitz S., Bender R., Snigula J., 2008, preprint (arXiv:0811.3211)
Brough S., Couch W. J., Collins C. A., Jarrett T., Burke D. J., Mann R. G., 2008, MNRAS, 385, L103
Bruzual G., Charlot S., 2003, MNRAS, 344, 1000
Burke C., Collins C. A., 2013, MNRAS, 434, 2856
Capasso R. et al., 2019, MNRAS, 482, 1043
Cassano R., Ettori S., Giacintucci S., Brunetti G., Markevitch M., Venturi T., Gitti M., 2010, ApJ, 721, L82
Cialone G., De Petris M., Sembolini F., Yepes G., Baldi A. S., Rasia E., 2018, MNRAS, 477, 139
de los Rios M., Domínguez R. M. J., Paz D., Merchán M., 2016, MNRAS, 458, 226
De Propris R., Phillipps S., Bremer M. N., 2013, MNRAS, 434, 3469
DES Collaboration, 2016, MNRAS, 460, 1270
Drabent A., Hoeft M., Pizzo R. F., Bonafede A., van Weeren R. J., Klein U., 2015, A&A, 575, A8
Drlica-Wagner A. et al., 2018, ApJS, 235, 33
Duffy A. R., Schaye J., Kay S. T., Dalla Vecchia C., 2008, MNRAS, 390, L64
Ebeling H., Edge A. C., Henry J. P., 2001, ApJ, 553, 668
Eckert D., Gaspari M., Vazza F., Gastaldello F., Tramacere A., Zimmer S., Ettori S., Paltani S., 2017, ApJ, 843, L29
Edwards L. O. V., Patton D. R., 2012, MNRAS, 425, 287
Ensslin T. A., Biermann P. L., Klein U., Kohle S., 1998, A&A, 332, 395
Feretti L., Giovannini G., Govoni F., Murgia M., 2012, A&AR, 20, 54
Flaugher B. et al., 2015, AJ, 150, 150
Freeman P. E., Kashyap V., Rosner R., Lamb D. Q., 2002, ApJS, 138, 185

Harvey D., Massey R., Kitching T., Taylor A., Tittley E., 2015, Science, 347, 1462
Hasselfield M. et al., 2013, J. Cosmol. Astropart. Phys., 2013, 008
Hennig C. et al., 2017, MNRAS, 467, 4015
Hollowood D. L. et al., 2019, ApJS, 244, 22
Hoshino H. et al., 2015, MNRAS, 452, 998
Hudson D. S., Mittal R., Reiprich T. H., Nulsen P. E. J., Andernach H., Sarazin C. L., 2010, A&A, 513, A37
Jeltema T. E., Canizares C. R., Bautz M. W., Buote D. A., 2005, ApJ, 624, 606
Khullar G. et al., 2019, ApJ, 870, 7
Kim S. Y., Peter A. H. G., Wittman D., 2017, MNRAS, 469, 1414
Lidman C. et al., 2012, MNRAS, 427, 550
Lidman C. et al., 2013, MNRAS, 433, 825
Lin Y.-T., Mohr J. J., 2004, ApJ, 617, 879
Lin Y.-T., Mohr J. J., Stanford S. A., 2004, ApJ, 610, 745
Lloyd-Davies E. J. et al., 2011, MNRAS, 418, 14
Lopes P. A. A., Trevisan M., Laganá T. F., Durret F., Ribeiro A. L. B., Rembold S. B., 2018, MNRAS, 478, 5473
López-Cruz O., Barkhouse W. A., Yee H. K. C., 2004, ApJ, 614, 679
Lotz J. M. et al., 2013, ApJ, 773, 154
Lovisari L. et al., 2017, ApJ, 846, 51
Ma C.-J., Ebeling H., Marshall P., Schrabback T., 2010, MNRAS, 406, 121
McDonald M. et al., 2012, Nature, 488, 349
McDonald M. et al., 2013, ApJ, 774, 23
McDonald M. et al., 2014, ApJ, 794, 67
McDonald M. et al., 2016, ApJ, 817, 86
McDonald M., Gaspari M., McNamara B. R., Tremblay G. R., 2018, ApJ, 858, 45
McDonald M. et al., 2019, ApJ, 870, 85
McPartland C., Ebeling H., Roediger E., Blumenthal K., 2016, MNRAS, 455, 2994
Mann A. W., Ebeling H., 2012, MNRAS, 420, 2120
Markevitch M., Vikhlinin A., 2007, Phys. Rep., 443, 1
Markevitch M., Gonzalez A. H., Clowe D., Vikhlinin A., Forman W., Jones C., Murray S., Tucker W., 2004, ApJ, 606, 819
Martinet N., Durret F., Adami C., Rudnick G., 2017, A&A, 604, A80
Martínez H. J., Zandivarez A., 2012, MNRAS, 419, L24
Mohr J. J., Fabricant D. G., Geller M. J., 1993, ApJ, 413, 492
Monteiro-Oliveira R., Cypriano E. S., Vitorelli A. Z., Ribeiro A. L. B., Sodré L., Dupke R., Mendes de Oliveira C., 2018, MNRAS, 481, 1097
Morganson E. et al., 2018, PASP, 130, 074501
Nelson K., Lau E. T., Nagai D., Rudd D. H., Yu L., 2014, ApJ, 782, 107
Ng K. Y., Pillepich A., Wittman D., Dawson W. A., Hernquist L., Nelson D. R., 2017, preprint (arXiv:1703.00010)
Nurgaliev D., McDonald M., Benson B. A., Miller E. D., Stubbs C. W., Vikhlinin A., 2013, ApJ, 779, 112
Nurgaliev D. et al., 2017, ApJ, 841, 5
Oguri M., Takada M., Okabe N., Smith G. P., 2010, MNRAS, 405, 2215
Owers M. S., Couch W. J., Nulsen P. E. J., Randall S. W., 2012, ApJ, 750, L23
Parekh V., van der Heyden K., Ferrari C., Angus G., Holwerda B., 2015, A&A, 575, A127
Pinzke A., Pfrommer C., 2010, MNRAS, 409, 449
Pipino A., Szabo T., Pierpaoli E., MacKenzie S. M., Dong F., 2011, MNRAS, 417, 2817
Planck Collaboration IX, 2011, A&A, 536, A9
Planck Collaboration XX, 2014, A&A, 571, A20
Planck Collaboration XXVII, 2016, A&A, 594, A27
Pranger F. et al., 2013, A&A, 557, A62
Pranger F., Böhm A., Ferrari C., Maurogordato S., Benoist C., Höller H., Schindler S., 2014, A&A, 570, A40
Rasia E., Meneghetti M., Ettori S., 2013, Astron. Rev., 8, 40
Reiprich T. H., Böhringer H., 2002, ApJ, 567, 716
Ribeiro A. L. B., Lopes P. A. A., Rembold S. B., 2013, A&A, 556, A74
Romer K., Viana P. T. P., Liddle A. R., Mann R. G., 2000, in Plionis M., Georgantopoulos I., eds, Large ScaleStructure in the X-ray Universe, Proceedings of the 20-22 September 1999 Workshop, Santorini, Greece, Atlantisciences, Paris, France, p. 409
Rossetti M. et al., 2016, MNRAS, 457, 4515
Rozo E., Rykoff E. S., 2014, ApJ, 783, 80
Rykoff E. S. et al., 2014, ApJ, 785, 104
Sarazin C. L., 2002, in Feretti L., Gioia I. M., Giovannini G., eds, Astrophysics and Space Science Library, Vol. 272, Merging Processes in Galaxy Clusters. Springer Netherlands, Dordrecht, p. 1
Saro A. et al., 2015, MNRAS, 454, 2305
Schechter P., 1976, ApJ, 203, 297
Semler D. R. et al., 2012, ApJ, 761, 183
Sifón C. et al., 2013, ApJ, 772, 25
Song J. et al., 2012, ApJ, 761, 22
Story K. et al., 2011, ApJ, 735, L36
Strazzullo V. et al., 2019, A&A, 622, A117
Takizawa M., Nagino R., Matsushita K., 2010, PASJ, 62, 951
Thompson R., Davé R., Nagamine K., 2015, MNRAS, 452, 3030
Tran K.-V. H., Kelson D. D., van Dokkum P., Franx M., Illingworth G. D., Magee D., 1999, ApJ, 522, 39
Tremaine S., 1990, in Wielen R., ed., The Origin of Central Cluster Galaxies, Springer Berlin, Heidelberg, p. 394
van Dokkum P. G., Franx M., Fabricant D., Kelson D. D., Illingworth G. D., 1999, ApJ, 520, L95
van Weeren R. J., 2011, PhD thesis, Leiden Observatory, The Netherlands
van Weeren R. J. et al., 2017, Nat. Astron., 1, 0005
Watson C. et al., 2019, ApJ, 874, 63
Wen Z. L., Han J. L., 2013, MNRAS, 436, 275
Wen Z. L., Han J. L., 2015, MNRAS, 448, 2
Zenteno A. et al., 2011, ApJ, 734, 3
Zenteno A. et al., 2016, MNRAS, 462, 830 (Z16)
Zitrin A., Broadhurst T., Barkana R., Rephaeli Y., Benítez N., 2011, MNRAS, 410, 1939
Zitrin A., Bartelmann M., Umetsu K., Oguri M., Broadhurst T., 2012, MNRAS, 426, 2944
Zitrin A. et al., 2013, ApJ, 762, L30

[1]*Cerro Tololo Inter-American Observatory, NSF's National Optical-Infrared Astronomy Research Laboratory, Casilla 603, La Serena, Chile*
[2]*Faculty of Physics, Ludwig-Maximilians-Universität, Scheinerstr 1, D-81679 Munich, Germany*
[3]*Gemini Observatory, NSF's National Optical-Infrared Astronomy Research Laboratory, Casilla 603, La Serena, Chile*
[4]*Max Planck Institute for Extraterrestrial Physics, Giessenbachstrasse, D-85748 Garching, Germany*
[5]*Department of Physics and Astronomy, University of Sussex, Pevensey Building, Brighton BN1 9QH, UK*
[6]*Santa Cruz Institute for Particle Physics, Santa Cruz, CA 95064, USA*
[7]*Fermi National Accelerator Laboratory, PO Box 500, Batavia, IL 60510, USA*
[8]*Kavli Institute for Cosmological Physics, University of Chicago, Chicago, IL 60637, USA*
[9]*Astronomy Unit, Department of Physics, University of Trieste, via Tiepolo 11, I-34131 Trieste, Italy*
[10]*IFPU – Institute for Fundamental Physics of the Universe, Via Beirut 2, I-34014 Trieste, Italy*
[11]*INAF – Osservatorio Astronomico di Trieste, via G. B. Tiepolo 11, I-34143 Trieste, Italy*
[12]*Department of Physics, Stanford University, 382 Via Pueblo Mall, Stanford, CA 94305, USA*
[13]*Kavli Institute for Particle Astrophysics & Cosmology, Stanford University, PO Box 2450, Stanford, CA 94305, USA*
[14]*SLAC National Accelerator Laboratory, Menlo Park, CA 94025, USA*
[15]*Departamento de Fisica y Astronomia, Universidad de La Serena, Avenida Juan Cisternas 1200, La Serena, 1720236, Chile*
[16]*Department of Geography, Ludwig-Maximilians-Universität, Luisenstr 37, D-80333 Munich, Germany*

[17]*The Research School of Astronomy and Astrophysics, Australian National University, Canberra, ACT 2601, Australia*
[18]*Departamento de Física Matemática, Instituto de Física, Universidade de São Paulo, CP 66318, São Paulo, SP 05314-970, Brazil*
[19]*Laboratório Interinstitucional de e-Astronomia – LIneA, Rua Gal. José Cristino 77, Rio de Janeiro, RJ 20921-400, Brazil*
[20]*Instituto de Fisica Teorica UAM/CSIC, Universidad Autonoma de Madrid, E-28049 Madrid, Spain*
[21]*Department of Physics, University of Cincinnati, Cincinnati, OH 45221, USA*
[22]*CNRS, Institut d'Astrophysique de Paris, UMR 7095, F-75014 Paris, France*
[23]*Institut d'Astrophysique de Paris, Sorbonne Universités, UPMC Univ Paris 06, UMR 7095, F-75014 Paris, France*
[24]*Department of Physics & Astronomy, University College London, Gower Street, London WC1E 6BT, UK*
[25]*Oskar Klein Centre, Department of Physics, Stockholm University, AlbaNova University Centre, SE 106 91 Stockholm, Sweden*
[26]*Centro de Investigaciones Energéticas, Medioambientales y Tecnológicas (CIEMAT), 40 - 28040 Madrid, Spain*
[27]*Department of Astronomy, University of Illinois at Urbana-Champaign, 1002 W. Green Street, Urbana, IL 61801, USA*
[28]*National Center for Supercomputing Applications, 1205 West Clark St, Urbana, IL 61801, USA*
[29]*Institut de Física d'Altes Energies (IFAE), The Barcelona Institute of Science and Technology, Campus UAB, E-08193 Bellaterra (Barcelona), Spain*
[30]*Institut d'Estudis Espacials de Catalunya (IEEC), E-08034 Barcelona, Spain*
[31]*Institute of Space Sciences (ICE, CSIC), Campus UAB, Carrer de Can Magrans, s/n, E-08193 Barcelona, Spain*
[32]*Institute for Fundamental Physics of the Universe, Via Beirut 2, I-34014 Trieste, Italy*
[33]*Observatório Nacional, Rua Gal. José Cristino 77, Rio de Janeiro, RJ 20921-400, Brazil*
[34]*Department of Physics, IIT Hyderabad, Kandi, Telangana 502285, India*
[35]*Department of Astronomy/Steward Observatory, University of Arizona, 933 North Cherry Avenue, Tucson, AZ 85721-0065, USA*
[36]*Jet Propulsion Laboratory, California Institute of Technology, 4800 Oak Grove Dr., Pasadena, CA 91109, USA*
[37]*Department of Astronomy, University of Michigan, Ann Arbor, MI 48109, USA*
[38]*Department of Physics, University of Michigan, Ann Arbor, MI 48109, USA*
[39]*Department of Physics and Astronomy, University of Missouri, 5110 Rockhill Road, Kansas City, MO 64110, USA*
[40]*Department of Astronomy, University of Michigan, 1085 S. University, Ann Arbor, MI 48109, USA*
[41]*Département de Physique Théorique and Center for Astroparticle Physics, Université de Genève, 24 quai Ernest Ansermet, CH-1211 Geneva, Switzerland*
[42]*Department of Physics, ETH Zurich, Wolfgang-Pauli-Strasse 16, CH-8093 Zurich, Switzerland*
[43]*School of Mathematics and Physics, University of Queensland, Brisbane, QLD 4072, Australia*
[44]*Center for Cosmology and Astro-Particle Physics, The Ohio State University, Columbus, OH 43210, USA*
[45]*Department of Physics, The Ohio State University, Columbus, OH 43210, USA*
[46]*Center for Astrophysics | Harvard & Smithsonian, 60 Garden Street, Cambridge, MA 02138, USA*
[47]*Australian Astronomical Optics, Macquarie University, North Ryde, NSW 2113, Australia*
[48]*Lowell Observatory, 1400 Mars Hill Rd, Flagstaff, AZ 86001, USA*
[49]*Kavli Institute for Astrophysics and Space Research, Massachusetts Institute of Technology, 77 Massachusetts Avenue, Cambridge, MA 02139, USA*
[50]*Department of Physics and Astronomy, University of Pennsylvania, Philadelphia, PA 19104, USA*
[51]*Department of Astrophysical Sciences, Princeton University, Peyton Hall, Princeton, NJ 08544, USA*
[52]*Institució Catalana de Recerca i Estudis Avançats, E-08010 Barcelona, Spain*
[53]*Institute of Astronomy, University of Cambridge, Madingley Road, Cambridge CB3 0HA, UK*
[54]*School of Physics and Astronomy, University of Southampton, Southampton SO17 1BJ, UK*
[55]*Physics Department, Brandeis University, 415 South Street, Waltham, MA 02453, USA*
[56]*Computer Science and Mathematics Division, Oak Ridge National Laboratory, Oak Ridge, TN 37831, USA*
[57]*Institute of Cosmology and Gravitation, University of Portsmouth, Portsmouth PO1 3FX, UK*

This paper has been typeset from a TEX/LATEX file prepared by the author.